

# Geochemistry, Geophysics, Geosystems®

## RESEARCH ARTICLE

10.1029/2022GC010738

### Key Points:

- Anisotropic Rayleigh and Love wave tomography of the Cascades arc reveals two distinct arc parallel magma reservoirs in the mid-lower crust
- One connecting Mt. Rainier to Mt. Adams (MA) and another Mt. St. Helens (MSH) to Mt. Hood with ~50 km offset at the latitudes of MA and MSH
- Positive anisotropy adjacent to the magma reservoirs may represent and is interpreted as sill complexes with mostly crystallized mafic magma

### Supporting Information:

Supporting Information may be found in the online version of this article.

### Correspondence to:

C. Jiang,  
chengxin.jiang1@anu.edu.au

### Citation:

Jiang, C., Schmandt, B., Abers, G. A., Kiser, E., & Miller, M. S. (2023). Segmentation and radial anisotropy of the deep crustal magmatic system beneath the Cascades arc. *Geochemistry, Geophysics, Geosystems*, 24, e2022GC010738. <https://doi.org/10.1029/2022GC010738>

Received 13 OCT 2022  
Accepted 6 FEB 2023

### Author Contributions:

**Conceptualization:** Chengxin Jiang, Brandon Schmandt  
**Formal analysis:** Chengxin Jiang, Eric Kiser  
**Funding acquisition:** Brandon Schmandt, Meghan S. Miller  
**Methodology:** Chengxin Jiang  
**Supervision:** Brandon Schmandt, Geoffrey A. Abers  
**Visualization:** Chengxin Jiang, Brandon Schmandt, Geoffrey A. Abers, Eric Kiser, Meghan S. Miller

© 2023 The Authors.

This is an open access article under the terms of the Creative Commons Attribution-NonCommercial License, which permits use, distribution and reproduction in any medium, provided the original work is properly cited and is not used for commercial purposes.

## Segmentation and Radial Anisotropy of the Deep Crustal Magmatic System Beneath the Cascades Arc

Chengxin Jiang<sup>1</sup> , Brandon Schmandt<sup>2</sup> , Geoffrey A. Abers<sup>3</sup> , Eric Kiser<sup>4</sup> , and Meghan S. Miller<sup>1</sup> 

<sup>1</sup>Research School of Earth Sciences, The Australian National University, Acton, ACT, Australia, <sup>2</sup>Department of Earth and Planetary Sciences, University of New Mexico, Albuquerque, NM, USA, <sup>3</sup>Department of Earth and Atmospheric Sciences, Cornell University, Ithaca, NY, USA, <sup>4</sup>Department of Geosciences, University of Arizona, Tucson, AZ, USA

**Abstract** Volcanic arcs consist of many distinct vents that are ultimately fueled by the common melting processes in the subduction zone mantle wedge. Seismic imaging of crustal-scale magmatic systems can provide insight into how melt is organized in the deep crust and eventually focused beneath distinct vents as it ascends and evolves. Here, we investigate the crustal-scale structure beneath a section of the Cascades arc spanning four major stratovolcanoes: Mt. Hood, Mt. St. Helens (MSH), Mt. Adams (MA), and Mt. Rainier, based on ambient noise data from 234 seismographs. Simultaneous inversion of Rayleigh and Love wave dispersion constrains the isotropic shear velocity ( $V_s$ ) and identifies radially anisotropic structures. Isotropic  $V_s$  shows two sub-parallel low- $V_s$  zones (~3.45–3.55 km/s) at ~15–30 km depth with one connecting Mt. Rainier to MA, and another connecting MSH to Mt. Hood, which are interpreted as deep crustal magma reservoirs containing up to ~2.5%–6% melt, assuming near-equilibrium melt geometry. Negative radial anisotropy, from vertical fractures like dikes, is prevalent in this part of the Cascadia, but is interrupted by positive radial anisotropy, from subhorizontal features like sills, extending vertically beneath MA and Mt. Rainier at ~10–30 km depth and weaker and west-dipping positive anisotropy beneath MSH. The positive anisotropy regions are adjacent to rather than co-located with the isotropic low- $V_s$  anomalies. Ascending melt that stalled and mostly crystallized in sills with possible compositional differences from the country rock may explain the near-average  $V_s$  and positive radial anisotropy adjacent to the active deep crustal magma reservoirs.

**Plain Language Summary** Volcanic arcs, a common result of subduction processes, comprise a large proportion of active volcanoes in the world and pose significant hazards. Seismic tomography measures variations of seismic wave speed in the subsurface, which can then be used to infer important properties of the volcanic systems, such as the distribution and configuration of active melts in the crust. In this study, we use continuous seismic data from 234 seismography in the Cascades arc and measure the wave speed of two types of surface waves, Rayleigh and Love waves. This allows us to infer not only the averaged shear-wave speed of the subsurface structures, but also its direction dependence, a seismic property known as seismic anisotropy. Our results show two concentrated and arc parallel low-velocity anomalies at 15–30 km depth beneath the arc: one connecting Mt. Rainier to Mt. Adams, and another connecting Mt. St. Helens to Mt. Hood. We interpret these low-velocity zones as deep crustal magma reservoirs with up to ~2.5%–6% melt. We identify positive radial anisotropy adjacent to the isotropic low-velocity anomalies at a similar depth range, and interpret them as sill complexes with mostly crystallized magma extracted from laterally offset deep crustal reservoirs.

## 1. Introduction

Subduction zone plate boundaries extend for hundreds to thousands of kilometers along strike fueling volcanic arcs on the overriding plate. Slab inputs to the mantle that are continuous along strike give rise to discrete volcanoes with variable distance from the plate boundary and along-strike spacing (e.g., Lee & Wada, 2017; O’Hara et al., 2020) as well as compositional heterogeneity within and between different volcanoes (e.g., Pitcher & Kent, 2019; Wanke et al., 2019). Heterogeneity also occurs at intermediate scales in which groups of adjacent volcanoes with common geochemical or eruptive characteristics define along-strike segments (O’Hara et al., 2020; Pitcher & Kent, 2019; Schmidt et al., 2008). It is unclear how these aspects of volcanic arc heterogeneity are linked to deep crustal magma reservoirs, which process mantle melt inputs into their eventual volcanic or intrusive products. Magma reservoirs beneath volcanic arcs are thought to span the entire crustal depth range and create long-lived hot zones, although the specific organization of melt accumulations is transient (Cashman

**Writing – original draft:** Chengxin Jiang, Brandon Schmandt

**Writing – review & editing:** Chengxin Jiang, Brandon Schmandt, Geoffrey A. Abers, Eric Kiser, Meghan S. Miller

et al., 2017). Here, we investigate the crustal-scale structure beneath an area including four stratovolcanoes of the Cascades arc extending northward from Mt. Hood to Mt. Rainier (Figure 1). The two intervening stratovolcanoes, Mt. St. Helens (MSH) and Mt. Adams (MA), are located at the same along-strike position but are separated by about 50 km in distance from the plate boundary. We seek to address the continuity of the deep crustal magma systems beneath these four stratovolcanoes using insights from the anisotropic shear velocity structure.

Recent studies have used regional surface wave tomography along with complementary geological constraints to investigate magmatic flux variations along the entire Cascades arc and at local scales. Till et al. (2019) show evidence for higher mantle melt flux into the crust beneath the southern to central Cascades compared to the central to northern Cascades, where volcanic centers are more spatially isolated. O’Hara et al. (2020) found that vent density is correlated with negative Rayleigh phase velocities, suggesting that upper to middle crustal structural attributes are linked to variable focusing of volcanism along the arc. The present study area, previously referred to as the Columbia segment of the Cascades arc (Schmidt et al., 2008), is located near the transition from more distributed vents and higher magmatic flux in the south to more localized vents and lower flux in the north (O’Hara et al., 2020).

Local isotropic shear velocity ( $V_s$ ) tomography has been conducted with subsets of the data used in this study and found that a relatively low  $V_s$  zone in the middle to lower crust spans much of the area between MSH, MA, and Mt. Rainier (Crosbie et al., 2019; Flinders & Shen, 2017). The absolute  $V_s$  of ~3.4–3.6 km/s in this zone is consistent with a small melt fraction but could alternatively be explained by some sub-solidus crustal compositions (Crosbie et al., 2019). It is unclear if this potential deep crustal magma reservoir connects southward beneath Mt. Hood. Why does the volcanic arc host two stratovolcanoes at the along-strike position of MSH and MA also remains poorly understood.

This study integrates ambient noise interferometry measurements from 234 temporary and permanent seismographs for simultaneous inversion of Rayleigh and Love wave dispersion for a local shear-wave model to gain new insights into the organization of the sub-arc magmatic system. A wide aperture of regional seismic network data combined with dense temporary array data avoids “edge effects” in the area of interest and provides a continuous view of the magmatic system from Mt. Hood to Mt. Rainier (Figure 1). Additionally, this study uses radially anisotropic surface wave tomography to constrain differences in vertically polarized shear velocity ( $V_{SV}$ ) and horizontally polarized shear velocity ( $V_{SH}$ ). Recent studies have shown distinctive radial anisotropic structure, with co-located low  $V_s$  and  $V_{SH} > V_{SV}$ , underlying volcanic systems in arc and intraplate settings with compositionally evolved magmas (Harmon & Rychert, 2015; Jaxybulatov et al., 2014; Jiang et al., 2018; Lynner et al., 2018; D. Miller et al., 2020). These results are consistent with the organization of melt into horizontally elongated sill-like volumes. Contrasting results with low  $V_s$  and  $V_{SV} > V_{SH}$  were found at Piton de la Fournaise, Reunion island, and Colima, Mexico, where primitive mafic sources dominate and more rapid transport through vertical dikes in the crust is hypothesized (Mordret et al., 2015; Spica et al., 2017). However, we note that the existing sampling of anisotropic structures beneath volcanic systems across the world might be biased. Many of the recent studies in volcanic fields with evolved compositions focused on voluminous systems, including those underlying the Toba caldera (Jaxybulatov et al., 2014), Yellowstone and Long Valley calderas (Jiang et al., 2018), and the Puna-Altiplano volcanic field (Lynner et al., 2018). Here, we seek to determine whether similar organization of anisotropy is observed at smaller scales beneath four stratovolcanoes of the Cascades arc.

## 2. Data and Method

### 2.1. Ambient Noise Data

Regional coverage is primarily provided by the EarthScope Transportable Array and permanent UW seismic networks (Figure 1), while temporary denser sampling is primarily provided by the imaging Magma Under St. Helens project’s XD network (Crosbie et al., 2019; Eakin et al., 2019; Ulberg et al., 2020) and the Cascadia Arrays for EarthScope (CAFE) project’s XU network (McGary et al., 2014). The XD network included 70 broadband seismic stations deployed within 50 km of MSH from June 2014 to August 2016. The XU network from the CAFE project included 60 broadband stations mostly along a transect slightly north of Mt. Rainier, along with some stations more broadly distributed in the forearc and arc. The distribution of all 234 stations is shown in Figure 1b and network information is given in Supporting Information S1. Many of the UW, TA, and other regional network stations were present during both dense temporary arrays, so there are abundant inter-station

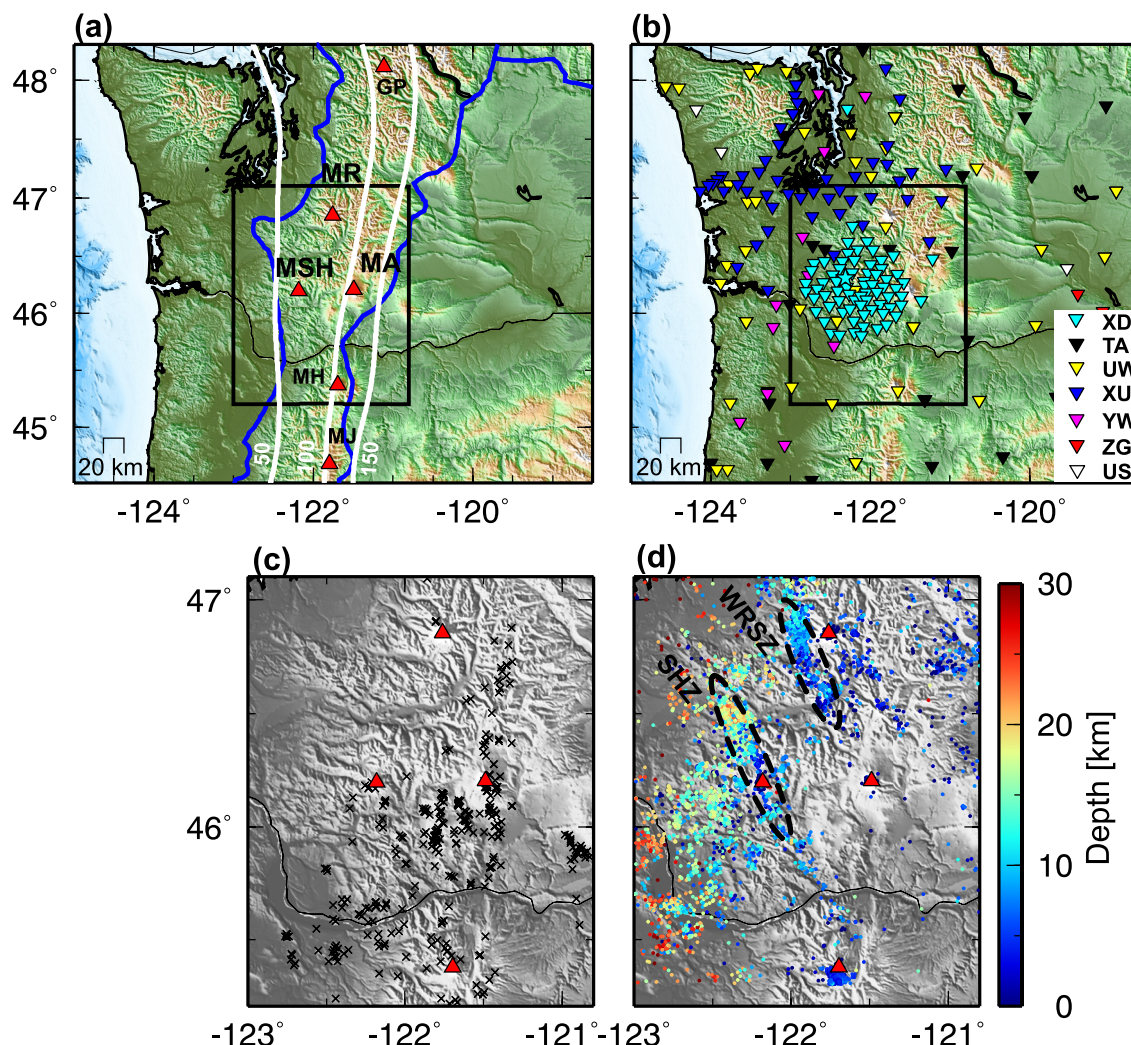


**Figure 1.** Tectonic context and station map. (a) Tectonic surroundings of the northern Cascades. The red triangles show the major Cascade arc volcanoes, including GP, Glacier Peak; MR, Mount Rainier; MSH, Mount St. Helens; MA, Mount Adam; MH, Mount Hood; MJ, Mount Jefferson. The blue lines denote the boundaries of the Cascade Volcanic Arcs. White lines show the 50, 100, and 150 km contours of the Juan de Fuca slab depth from Slab2 (Hayes et al., 2018). The black box outlines the focus region of this study as shown in Figures 7 and 8. (b) Seismic stations used in this study are color coded by the networks. The dense cyan triangles represent the imaging Magma Under St. Helens (XD) broadband array. Details of each network can be found in Table S1 in Supporting Information S1. (c) Quaternary vents (black crosses; Hildreth, 2007) in the focused region. (d) Local earthquakes (M1 and above from the Pacific Northwest Seismic Network) in the region color coded by depth. The St. Helens Seismic Zone (SHZ) and Western Rainier Seismic Zone (WRSZ) are indicated with black ellipses (Stanley et al., 1996).

paths connecting the dense arrays to the surrounding areas. During data preprocessing, the three-component continuous data were down-sampled to 1 Hz and the instrument response was removed.

## 2.2. Ambient Noise Processing

To process the noise data, we use the python package NoisePy (Jiang & Denolle, 2020), which is a high-performance tool designed specifically for large-scale ambient noise seismology. The main noise processing procedures in NoisePy generally follow the conventional workflow of Bensen et al. (2007). First, we downloaded three-component and day-long continuous data for each station and applied a taper and a 4-pole 2-pass Butter-worth filter from 0.02 to 0.5 Hz. We then downsampled them to 1 Hz before removing the mean, trend, and instrumental responses. Second, we further cut the daily data into 30-min segments with 75% overlap between adjacent windows to increase the signal-to-noise ratio of the stacked cross-correlation functions (CCFs; Seats et al., 2012). To reduce contamination from large transient signals, we removed segments with maximum amplitude  $>10$  times the standard deviation of the amplitude for each day. During this step, the mean and trend of the

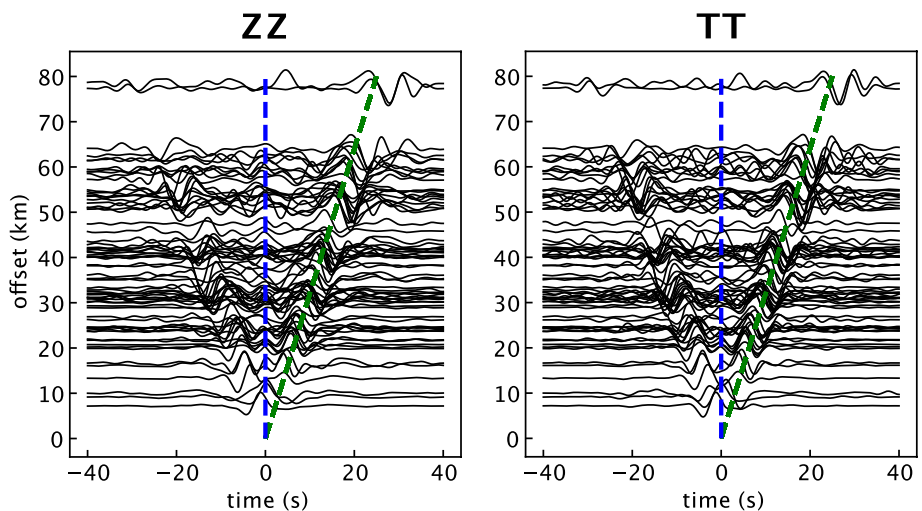


**Figure 2.** Move-out plot the ZZ and TT components of the correlation tensors between the source station XD.MG05 (marked as a star in Figure 1b) and the stations within 80 km radius (in the black box of Figure 1b). The waveforms are filtered at 0.05–0.25 Hz frequency band. The blue dashed lines denote time zero and the green dashed lines show a group velocity of 3.2 km/s.

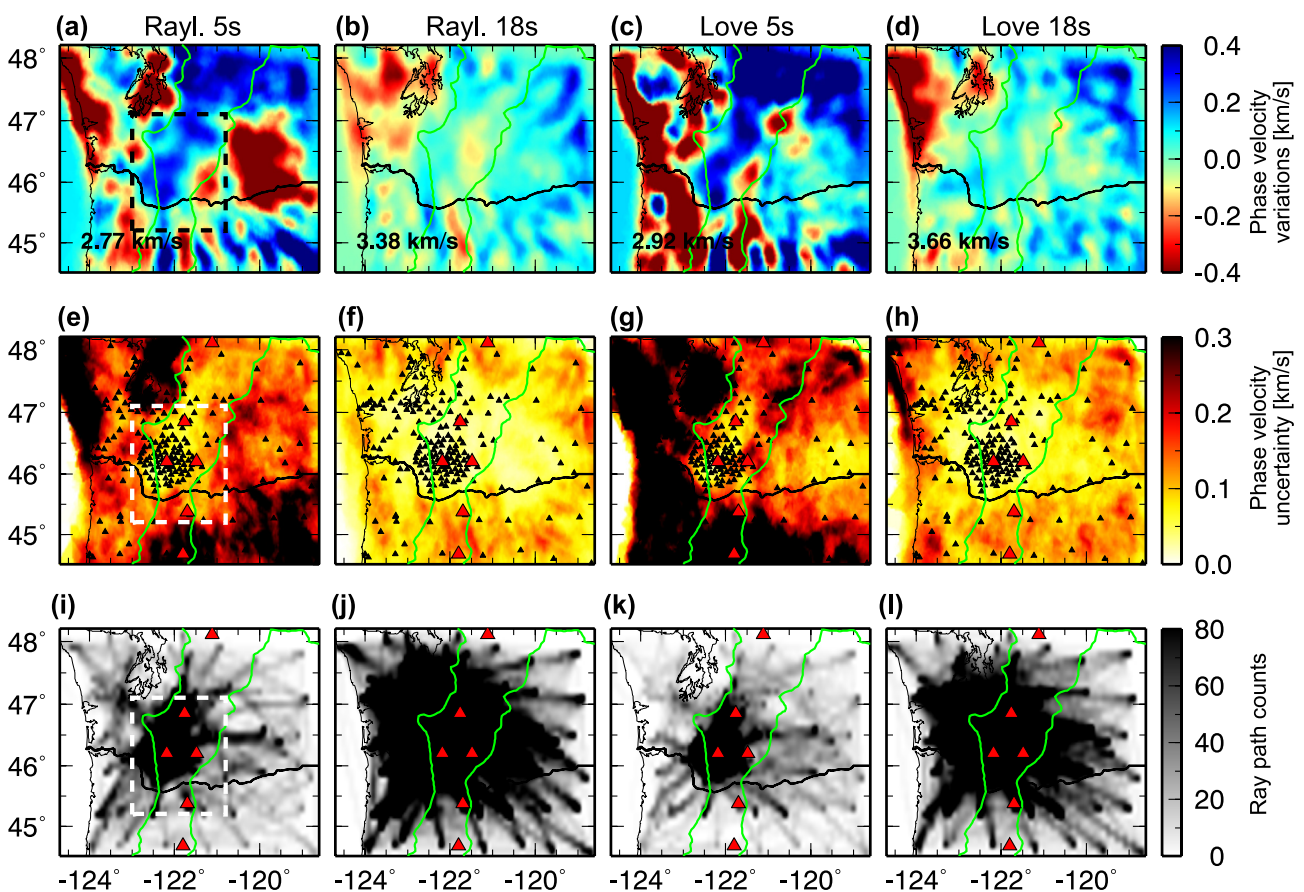
remaining time-series were removed again before applying a taper. The cross-correlation is then calculated in the frequency domain and a moving average with a window length of 20 samples ( $\sim 0.011$  Hz) is used to smooth the source and receiver spectra. Finally, we linearly stacked the cross correlations of the small-time windows for each station-pair, making  $>8,000$  stacked CCFs.

Figure 2 shows move-out plots for the vertical (ZZ) and transverse (TT) components of the correlation tensors filtered from 0.05 to 0.25 Hz, with a source station (XD.MG05) located close to MSH and receivers that are synchronous with the XD array. Rayleigh and Love waves travel at similar group velocities of about 3.2 km/s in this broad frequency range around MSH. The move-out plot also displays a weakly asymmetric pattern with the stronger positive lag signals reflecting stronger noise sources from the Pacific Ocean west of the array. Figure S1 in Supporting Information S1 include a move-out plot for the same source but with the complete nine-component tensors, which show the Rayleigh and Love wave energies are mostly propagating in plane.

To reduce the effects of inhomogeneous noise source distribution, as suggested by Lin et al. (2008), we averaged the positive and negative lags of the CCFs to obtain symmetric cross correlations. Frequency-Time analysis (FTAN) (Levshin & Ritzwoller, 2001) was applied to the symmetric Z-Z and T-T components to measure Rayleigh and Love wave dispersion from 2 to 40 s period. The GDM52 model from Ekström (2011) was used as an initial reference for FTAN to guide phase velocity picking at longer periods ( $>25$  s). Then, an updated reference dispersion curve based on the regional average was used to refine phase velocity estimates. Finally, we applied quality control (QC) criteria: (a) signal-to-noise ratio of the CCFs  $>8$  (Bensen et al., 2007) and (b) interstation distance  $>1.5$  wavelengths (Luo et al., 2015). We then inverted the phase velocity maps three times, removing travel times with misfits beyond two standard deviations after the first two inversions. Figure S2 in Supporting Information S1 summarizes the final dispersion measurements at each period.

### 2.3. Surface Wave Tomography

Dispersion measurements that passed the QC criteria were inverted for 2D phase velocity maps. Least squares travel time inversions using fixed spatial parameters and regularized with damping and smoothing tend to give poor amplitude resolution (e.g., Fang et al., 2020). To mitigate this challenge, we use a Poisson Voronoi (PV) projection-based tomography method, which projects the original 2D/3D space on a regular grid into low-dimensional subspaces formed by PV cells. In each subspace, the low-dimension image is efficient to optimize, making it computationally practical to avoid explicit regularization. Fang et al. (2020) demonstrated that the inverse problem in the projected subspace is better constrained due to the independence of each subspace. By conducting such inversions many times, each with a random distribution of Voronoi cells, the final solution can



**Figure 3.** Phase velocity variations related to the regional average and associated uncertainties resulted from the Poisson Voronoi-based tomography scheme at two selected periods of 5 and 18 s for Rayleigh and Love waves. The texts in the lower left of panels (a–d) indicate the regionally averaged phase velocity. The black triangles in panels (e–h) show the station distribution. The green lines denote the tectonic boundaries of the Cascade volcanic arcs. The dashed lines in panels (a, e, i) outline the phase velocity maps shown in Figure 5. The red triangles in panels (e–l) show the major Cascade arc volcanoes.

be obtained by averaging all solutions from low-dimensional subspaces. The ensemble solution also quantifies model parameter uncertainties.

Phase velocity map inversions were conducted for Rayleigh waves at 3–40 s and Love waves at 3–36 s periods (Figures S3 and S4 in Supporting Information S1). The 2D model space at each period was parameterized with 350 Voronoi cells. We conducted 70 low-dimensional inversions and used their average and standard deviation as the final model. The number of Voronoi cells and low-dimensional inversions have minor effects on the inversion results once they are within a certain range and our additional tests summarized in Figures S5 and S6 in Supporting Information S1 justify the use of these selected numbers for this study. During each low-dimensional inversion, the travel time wavefield is calculated using the ray-based pyKonal package (White et al., 2020). The wavefield is evaluated on a  $0.02^\circ \times 0.02^\circ$  grid augmented with five times denser sampling near the virtual source and receiver. In each subspace, the low-dimensional problem is optimized with the least-square method without regularization. The phase velocity maps and uncertainties at two example periods of 5 and 18 s are shown in Figure 3, with the travel time residuals before and after the inversion shown in Figure S7 in Supporting Information S1.

The example phase velocity maps in Figure 3 display a series of interesting velocity features in the study region. At a short period of 5 s (Figures 3a and 3c), phase velocities are mainly sensitive to shallow crustal structures confined to the uppermost  $\sim 8$  km. Similar patterns are observed for Rayleigh and Love waves, though Love waves travel slightly faster on average. The most prominent feature is that the Cascades arc exhibits higher phase velocities compared to the surrounding regions. Interestingly, south of  $47^\circ\text{N}$  the arc tends to separate into two distinct anomalies with the eastern half showing lower velocities compared to the western half (Figures 3a and 3c). The

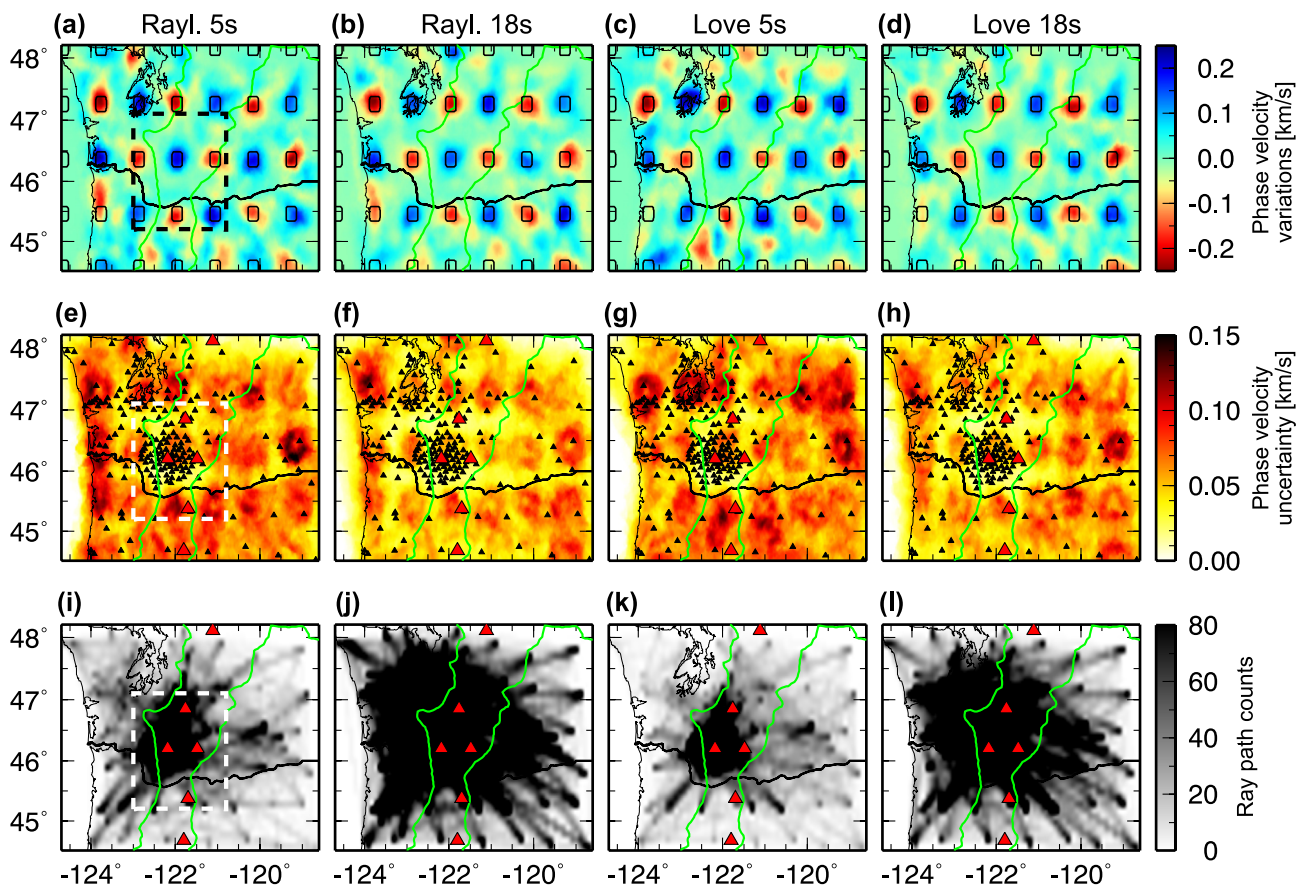


**Figure 4.** Sensitivity tests and raypath coverage for Rayleigh and Love wave phase velocity map inversion. Panels (a, e, i) inversion result, the associated uncertainty estimate and raypath coverage for 5 s Rayleigh wave; panels (b, f, j) same as the first column but for 18 s Rayleigh wave; panels (c, g, k) same as the first column but for 5 s Love wave; and panels (d, h, l) same as the first column but for 18 s Love wave. The black boxes in the upper panel denote the 0.25 km/s contour, representing the absolute values of the input model relative to the average. The thick dashed lines in panels (a, e, i) show the focus region of this study. The black triangles in panels (e–h) show the station distribution. The green lines denote the tectonic boundaries of the Cascades volcanic arc and the red triangles in panels (e–l) show the major Cascades arc volcanoes.

uncertainty maps in Figures 3e and 3g reveal that regions of denser path coverage (Figures 3i and 3k), such as near MSH, and show smaller uncertainties as expected.

The phase velocity map at 18 s period (Figures 3b and 3d) has smaller and more uniform uncertainties (Figures 3f and 3h) because the regional stations provide relatively high-density path coverage across the study area (Figures 3j and 3l). Phase velocities at this period reflect a blend of structures at middle crust depths of ~10–25 km. The western portion of the Cascades arc continues to show higher velocities than the east (Figures 3b and 3d), although the contrast diminishes in amplitude. The associated uncertainty maps indicate that regions of small uncertainties extend to a much broader extent compared to those at 5 s period, but the model edges still show larger uncertainties due to diminishing ray coverage (Figures 3j and 3l).

#### 2.4. Sensitivity Tests

Phase velocity tomography sensitivity tests were conducted to assess the model resolution. We input a sparse distribution of spikes rather than the conventional checkerboard model to provide better insights into model reliability as suggested by Rawlinson and Spakman (2016). The model is constructed on the same geographic grid used for the observational data inversion. Spikes are set to have alternating positive and negative amplitudes of 10% relative to a background phase velocity of 3 km/s (Figure 4a). Each spike has a horizontal size of  $0.3^\circ \times 0.3^\circ$  and is separated by  $0.6^\circ$ . A 2D Gaussian filter with a mean of 0 and standard deviation of 1.5 is applied to smooth the model. Synthetic inter-station phase travel times are calculated using the same station pairs as in the observational

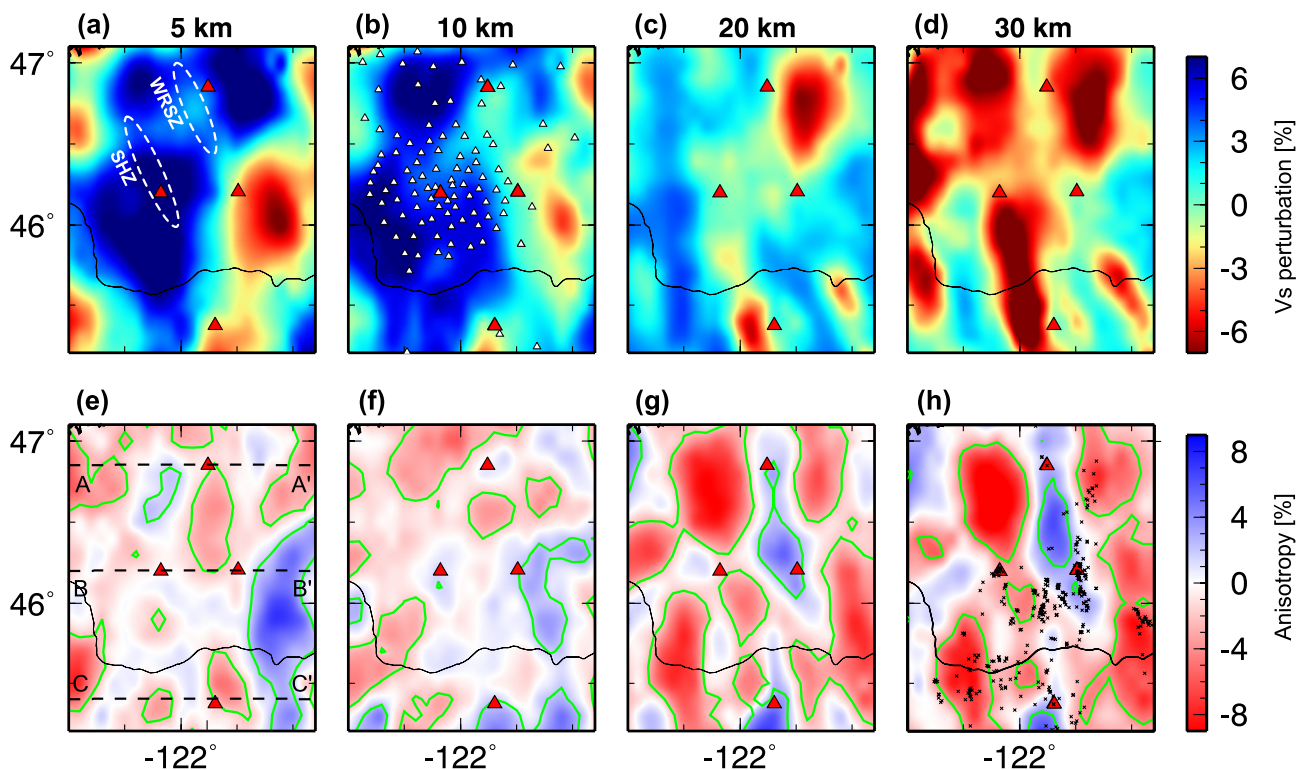


**Figure 5.** Map views of the 3D isotropic and anisotropic  $V_s$  model plotted at four selected depths of 5, 10, 20, and 30 km, respectively. White dashed ellipses in panel (a) delineate the WRSZ and SHZ, respectively. White triangles in panel (b) denote the seismic stations in the target area. The crosses in panel (h) denote the Quaternary vents (Hildreth, 2007). The black dashed lines in panel (e) denote the locations of the cross-section locations shown in Figure 8. The green lines in panels (e–h) outline the region of 65% confidence. The four red-filled triangles show the four major volcanoes in the region.

tomography with added random Gaussian noise with a standard deviation of 0.5 s, which is close to the travel time residuals of the tomography for the focused area. Then, the inversions are run with the same parameters as in the observational case. Figure 4 shows the input model and recovered Rayleigh wave phase velocity maps at 5 and 18 s, respectively. Similar results were obtained for Love wave sensitivity tests (Figure S4 in Supporting Information S1). Figure 4 indicates that PV-based tomography not only recovers the shape of the anomalies but also most of the true amplitude with a recovery rate of up to 80%. Meanwhile, the model does not show strong smearing effects even near edges, which commonly occurs in tomographic inversions relying on regularization. In addition, the PV-based tomography provides reasonable estimates of the model uncertainty, with large values clustered at regions of sparser path coverage.

## 2.5. Probabilistic Method to Derive 1D Anisotropic Profiles

Phase velocity maps are used as inputs for locally 1D  $V_s$  inversions, which are combined to form a 3D model. Local dispersion curves were extracted from the phase velocity maps at locations on a  $0.1^\circ \times 0.1^\circ$  grid for the region located within the black box of Figures 1a and 1b. Figure S8 in Supporting Information S1 shows the sensitivity kernels of Rayleigh and Love waves as a function of depth across the period range of real data, demonstrating good constraints of  $V_s$  to a depth of about 50 km. A Bayesian Markov-Chain Monte Carlo (McMC) inversion method based on Shen et al. (2013) was used to invert local 1D anisotropic  $V_s$  profiles on these grid points. The details of this inversion method can be found in Shen et al. (2013) and Jiang et al. (2018), and are briefly summarized below.

The McMC inversion precedes in three major steps. First, a series of parameters are selected to represent the model space, and the parameter ranges are set to form a prior distribution that spans the potential structural heterogeneity in the region. Second, Markov-chains of candidate models are constructed using parameters randomly selected from the prior distribution. Each Markov-chain evolves in a random walk fashion guided by the Metropolis algorithm (Mosegaard & Tarantola, 1995) and candidate models are evaluated using the  $\chi^2$  misfit between

the predicted dispersion curves and those from the observations, which are computed using subroutines from Computer Programs in Seismology (Herrmann, 2013). When an equilibrium in a model misfit is attained, a new Markov-chain is formed by randomly sampling the model space again. Finally, a 1D profile and uncertainties are generated using the mean and standard deviation of the distribution of the best-fitting models. The McMC inversion method outputs Probability Density Functions for each parameter, allowing further statistical analysis of the model solutions.

We explore the model space through a series of 1-D anisotropic  $V_s$  profiles that extend from the surface to 80 km depth and are represented by 13 free parameters. This includes five B-spline coefficients defining a continuous crustal  $V_s$ , another five B-spline coefficients forming the corresponding radial anisotropy profile in the crust, a parameter denoting the local Moho depth, and one isotropic and one anisotropic parameter representing the  $V_s$  and associated anisotropy in the upper mantle layer, respectively. The upper mantle layer extends from the local Moho to 80 km depth. Uniform prior distributions are used for all 13 parameters, with the prior distribution of the Moho depth locally centered within  $\pm 5$  km relative to the reference model of Schmandt et al. (2015) (Table S1 in Supporting Information S1). In this study, we define radial anisotropy following Equation 1 with  $V_s$  representing the average of  $V_{sv}$  and  $V_{sh}$ . Equation 1 also indicates that positive radial anisotropy means  $V_{sh} > V_{sv}$ .

$$\text{Aniso} = \frac{V_{sh} - V_{sv}}{V_s} \times 100\% \quad (1)$$

During the inversion,  $V_p$  and density of the 1D profile are scaled to  $V_s$  according to the empirical relations 1 and 9 of Brocher (2005). Attenuation effects on surface wave dispersion are corrected following Kanamori and Anderson (1977). In this study, each 1-D inversion contains 0.7 million iterations and the final average model is calculated from the mean of the best 2,000 models with the associated standard deviation approximating the corresponding model uncertainty. We conducted one synthetic test based on a realistic  $V_s$  profile from one example point beneath the Mount St. Helens to demonstrate that our inversion scheme and parameterization adopted here can constrain the depth-dependent isotropic and anisotropic parameters reasonably well (Figure S9 in Supporting Information S1).

We note that Moho models in the forearc and western Cascades differ among prior surveys as well as between passive and active methods. For example, controlled source P refraction and reflection imaging from Parsons et al. (1998) and Kiser et al. (2016) indicate  $\sim 40$  km thick crust between MSH and Mt. Rainier, while K. C. Miller et al. (1997) estimated a thicker crust,  $\sim 48$ – $50$  km in about the same location with sparser controlled source data coverage. A summary of Moho estimates from prior controlled source P-wave studies in the region is provided in Text S1 in Supporting Information S1. We choose a reference model of Schmandt et al. (2015), which is based on  $<0.5$  Hz Ps receiver functions and reveals  $\sim 40$  km regional crust, as their dominant sensitivity to low frequency shear velocity contrasts is consistent with our inversion of low frequency surface wave data. In addition, previous studies indicate that in areas where the Moho is complex, as the case in the western Cascades (Bostock, 2013; Brocher et al., 2003), methods such as teleseismic Ps receiver functions and surface wave dispersion may indicate the center of multi-layer transition or gradient. A more detailed justification for using the reference Moho model of Schmandt et al. (2015) is provided in Text S2 in Supporting Information S1.

### 3. Results

#### 3.1. 3D Isotropic Structure

The isotropic  $V_s$  model displays large velocity variations across the study area and throughout the crustal depth range (Figures 5 and 6), which are well beyond the associated uncertainties (Figure S10 in Supporting Information S1). The western half of the volcanic arc is characterized by  $V_s$   $\sim 5\%$ – $10\%$  higher than that of the eastern half at depths  $<10$  km (Figures 5a and 5b). The high velocities largely coincide with the Miocene position of the Cascades arc, which is located west of the active arc axis at the latitudes in the study area (R. E. Wells & McCaffrey, 2013). Exhumed intrusions are prevalent in surface exposures and inferred in the upper crust based on gravity, resistivity, and local earthquake travel time tomography (Bedrosian et al., 2018; Williams & Finn, 1987; Ulberg et al., 2020). The Columbia Basin east of MA is characterized by low velocities at depths  $<10$  km underlain by high-velocity anomalies in the lower crust (Figure 6c). We now focus on the detailed structures beneath the four volcanoes from the surface to the deep crust.

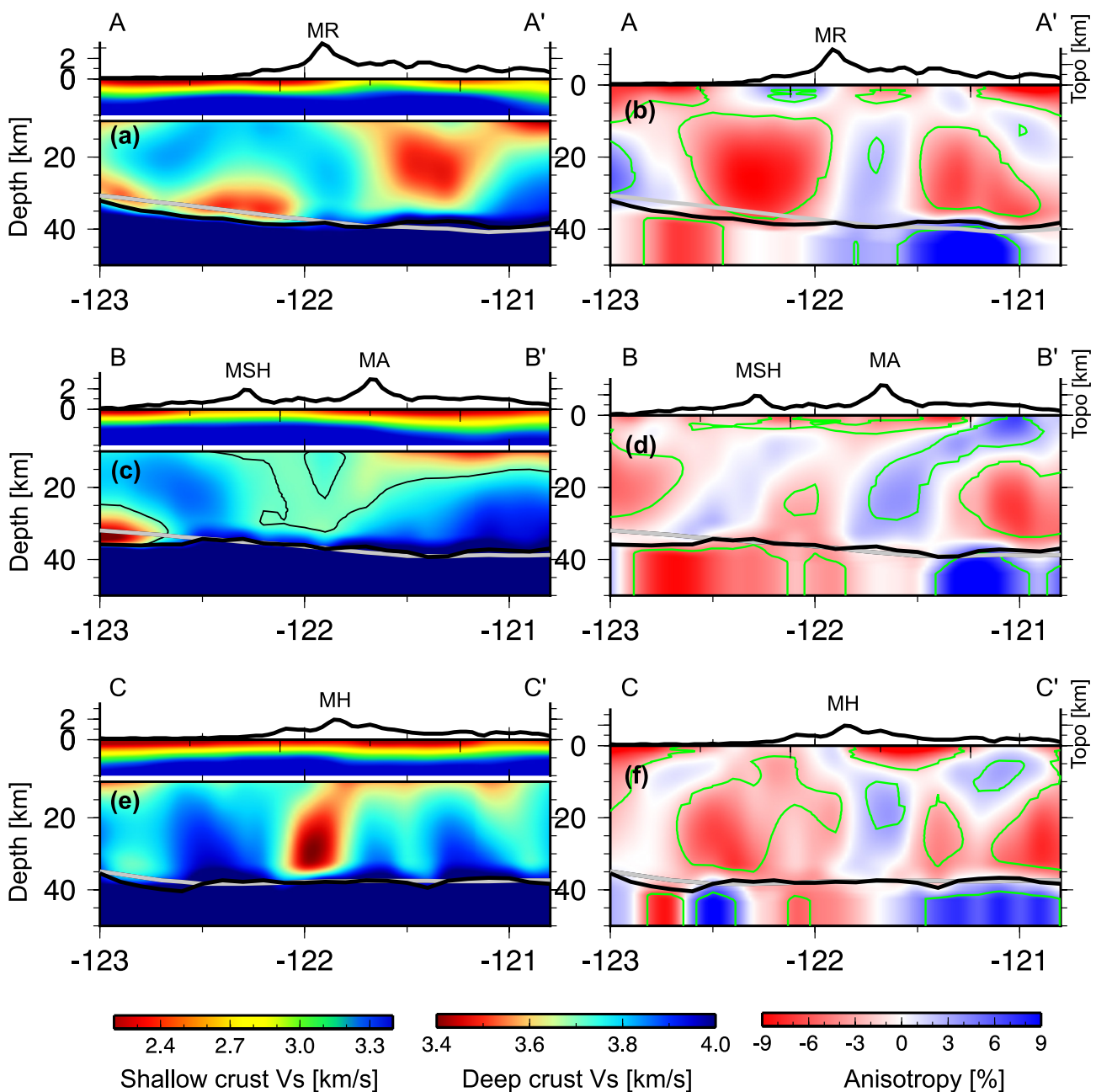


**Figure 6.** Vertical cross-sections of the 3D isotropic (a, c, e) and anisotropic (b, d, f)  $V_s$  model along the three profiles marked in Figure 5e. The topography variations are plotted at the top of each cross section. The crustal section of the isotropic  $V_s$  is broken into two components with different color bars to show the detailed velocity variations. The black lines in panel (c) show the velocity contour of 3.71 km/s. The thick gray lines illustrate the Moho variation from the reference model of Schmandt et al. (2015), while the thick black lines show the Moho variation from our inversion. The thin green lines in panels (b, d, f) outline the region of 65% confidence of non-zero radial anisotropy.

The upper crustal structure varies among the four major volcanoes. In the shallow crust beneath MSH,  $V_s$  is greater than the average in the study area, but at depths between 10 and 15 km, a small area of near-neutral velocity anomaly emerges (Figures 5a and 5b). The near-neutral velocity extends down to ~20 km depth, below which concentrated velocity reductions start to develop (Figures 5c and 5d). Beneath Mt. Rainier  $V_s$  is about ~4% faster than the average at 5 km depth and transitions to near neutral by 10 km depth (Figures 5a and 5b). In contrast, beneath MA and Mt. Hood anomalies of -3 to -6% are found a bit offset to the east but throughout the uppermost 10 km (Figures 5a and 5b). The higher upper crustal  $V_s$  beneath MSH and near average  $V_s$  at 10 km beneath Mt. Rainier may reflect a diluted signal of narrow magmatic systems embedded in the generally higher

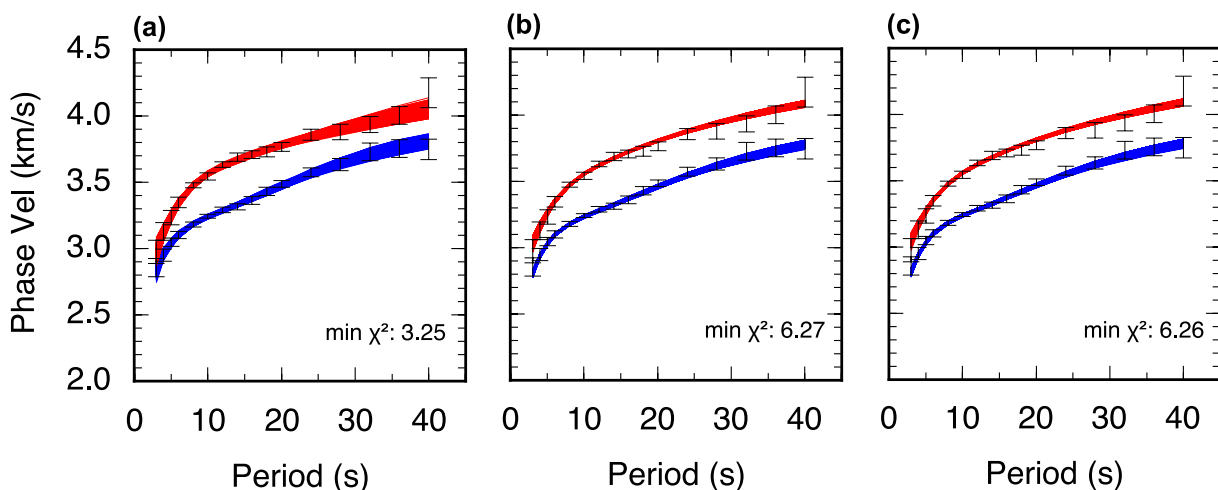


**Figure 7.** Rayleigh and Love wave dispersion fitting from the Bayesian Markov chain Monte Carlo inversion tests with three different parameterizations. The location is near the center of Mt. St. Helens ( $46.2^\circ\text{N}$ ,  $-122.2^\circ\text{E}$ ). The blue and red lines represent the ensemble of the predicted Rayleigh and Love wave dispersion from the best 2,000 models, and the 68% error bars from the 2D tomography. The number in the lower right indicates the minimum  $\chi^2$  misfit from each inversion. Panel (a) is for the inversion with the radially anisotropic parameterization described in Section 2.5. Panel (b) is for the inversion using 5 b-splines for  $V_s$  in the crust but no radial anisotropy parameters. Panel (c) is same as panel (b) except that 10 b-splines are used in the crust.

$V_s$  upper crust of the western Cascades arc. Higher frequency local earthquake and controlled source travel time tomography studies show localized low-velocity anomalies at  $\sim 5\text{--}10$  km depth beneath MSH and Mt. Rainier (Kiser et al., 2018; Moran et al., 1999; Ulberg et al., 2020).

In the mid-lower crust ( $\sim 15\text{--}30$  km), the most prominent result is that two elongated low-velocity zones (LVZs) underlie the arc and span the distance between major stratovolcanoes (Figures 5c and 5d): the northern LVZ follows the trend connecting Mt. Rainier to MA and the southern LVZ parallels the trend connecting MSH and Mt. Hood. Both LVZs have  $>5\%$  velocity reductions at  $>25$  km depth range and their horizontal positions are skewed to one side of each volcano. At 20 km depth (Figure 5c), the two LVZs display some weak connections where they nearly meet at the latitude of MSH and MA. The cross-section view (Figure 6b) shows that the low-velocity anomaly beneath the south side of MSH ( $3.65\text{--}3.71$  km/s) dips to the east and is separated from the west-dipping anomaly beneath MA by relatively high velocities ( $3.75\text{--}3.8$  km/s). The northern LVZ is wider and

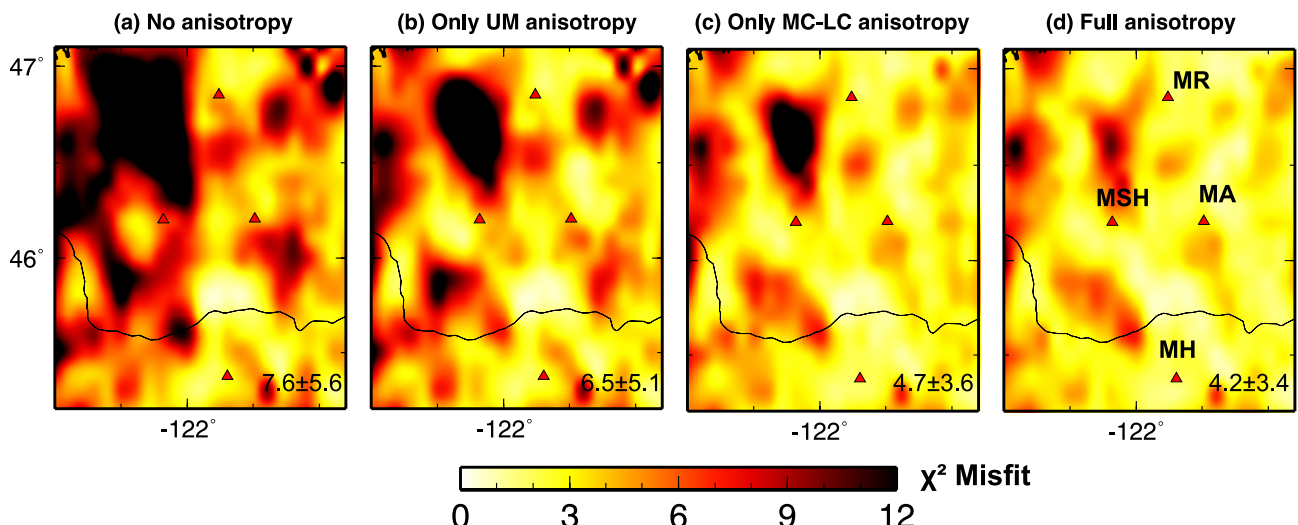


**Figure 8.**  $\chi^2$  misfit maps for the phase velocity measurements across the target region from four sets of inversions using different parameterizations. (a) Purely isotropic parameters; (b) only allowing upper mantle (UM) anisotropy; (c) only allowing mid-lower crust (MC-LC) anisotropy; and (d) allowing crust and upper mantle anisotropy. The pair of numbers in the lower right of each subplot represents the mean and standard deviation values of each corresponding misfit map. The red triangles mark the volcanoes of Mt. Rainier (MR), Mt. St. Helens (MSH), Mt. Adam (MA), and Mt. Hood (MH), respectively, as labeled in panel (d).

exhibits slightly lower  $V_s$  at 20 km depth (3.3–3.4 km/s), while the southern LVZ is narrower and more elongated sub-parallel to the arc (Figures 5d and 6).

Another interesting feature in the isotropic model is the considerably low velocities (3.2–3.3 km/s) in the lower-most crust of the northern forearc region (Figure 5d), which is also associated with large uncertainties compared to the surrounding areas (Figure S10 in Supporting Information S1). However, a similar LVZ was mapped by Delph et al. (2018) using surface waves and receiver functions to investigate the structure near the subduction interface. The LVZ may originate from underthrust sediments with fluids infiltrated from the slab (Delph et al., 2018). Based on active and passive seismic imaging and resistivity near southern Vancouver Island, Calvert et al. (2020) suggest that the ~6–10 km-thick LVZ may represent an overpressured shear zone, including underthrust rocks from the overriding forearc crust, imbricated upper oceanic crust, and intervening subducted sediments.

### 3.2. Evaluating the Significance of Radial Anisotropy

We first show an example location beneath MSH to demonstrate the importance of radial anisotropy parameters to simultaneously fit Rayleigh and Love dispersion. Three scenarios are considered for the 1D  $V_s$  inversion: the radially anisotropic parameterization described in Section 2.5, an isotropic inversion that maintains 5 b-splines for  $V_s$  in the crust but no radial anisotropy parameters, and another isotropic inversion with 10 b-splines in the crust (Figure 7). The first model using the preferred parameterization has a best  $\chi^2$  misfit of 3.2. The second inversion with the anisotropy parameters muted has a best  $\chi^2$  misfit of 6.2. The third case tests whether doubling the number of isotropic crustal b-spline parameters could achieve better results without requiring anisotropy; thus, it has the same number of parameters compared to that in the first case. Despite the increased number of parameters, the best  $\chi^2$  misfit is almost the same as for the isotropic model with only five crustal b-splines.

Given that the Rayleigh and Love wave dispersion data are much better fit by allowing radial anisotropy parameters in the example test introduced above, our next consideration is whether radial anisotropy parameters are needed in the depths relevant for the deep crustal magmatic system or just deeper and/or shallower in the model. To do this, we conducted four sets of inversions using the same dispersion data but with different McMC parameterizations. The four parameterizations are (I) isotropic crust and upper mantle, (II) isotropic crust and anisotropic upper mantle, (III) anisotropic mid-lower crust (splines 3–5) and anisotropic upper mantle, and (IV) anisotropic crust (splines 1–5) and upper mantle (Table S1 in Supporting Information S1). The performance of each set of the inversions is evaluated via the  $\chi^2$  misfit (Figure 8).

In general, assuming isotropic crust and upper mantle (model I) poorly fit the observations for most of the study area, with a mean  $\chi^2$  misfit of 7.6. Allowing anisotropy only in the upper mantle (model II) slightly leads to a slightly improved mean  $\chi^2$  misfit of 6.5. The introduction of anisotropy in the mid-lower crust (model III) results in greater improvement with mean  $\chi^2$  of 4.7. In addition, allowing anisotropy in the shallow crust on top of model III (model IV) further reduces the misfit to  $\chi^2$  of 4.2, making it our preferred model (Figure 7d).

### 3.3. 3D Radial Anisotropic Structure

The anisotropic component of the 3D model provides complementary information to the isotropic  $V_s$  structure. In general, the regional crust is characterized by broadly distributed negative anisotropy with an average amplitude of –3% to –4% shallower than 10 km depth (Figures 5e and 5f) increasing to –7% to –8% at depths greater than 15 km (Figures 5g and 5h). This is consistent with the large-scale western U.S. anisotropic model of Xie et al. (2015), in which our study region is the largest area showing negative anisotropy. The rest of the tectonically active western U.S. crust is dominated by positive radial anisotropy (Moschetti et al., 2010), which may be focused at middle crustal depths (Wilgus et al., 2020). The exact reason for the negative anisotropic feature in the crust beneath our study region remains to be explored, but indicates subvertical foliations or cracks. Potential mechanisms include the fossil fabrics from the accretionary history of the Cascadia block (R. Wells et al., 2014) and/or the widespread fracture/fault system for vertical fluid migration (R. E. Wells et al., 2017). Major volcanic systems are associated with anisotropic features that perturb the regionally prevalent negative anisotropy. We focus on the anomalies in the mid-lower crust as the anisotropy above ~6 km depth is more susceptible to potential bias introduced by the assumed  $V_p/V_s$  relation when scaling  $V_s$  to  $V_p$  for forward modeling as explained in Section 2.5.

At 10 km depth, moderate positive anisotropy (2%–3%) is observed beneath all four volcanoes, coinciding with areas of concentrated low-velocity anomalies. At 20–30 km depth, the anomalies beneath MA and Mt. Rainier

start to merge and form a narrower and stronger feature (4%–5%) parallel to the arc. Instead of sitting above the northern LVZ, this anisotropic feature is adjacent (Figures 5g and 5h). The positive anisotropy beneath MSH decays in amplitude and dips to the west (Figure 6d), while the southern LVZ between MSH and Mt. Hood exhibits its weak negative anisotropy (−2%–3%) at deeper depths.

While the upper mantle exhibits some strong anisotropic anomalies, our one-layer assumption in the inversion and potential complexity in this region makes it difficult to interpret. In general, negative anisotropy is more prevalent near the subduction zone and positive anisotropy is more prevalent in the back-arc (Figure 6d). Studies incorporating longer period data, such as teleseismic surface wave dispersion, could better constrain the upper mantle anisotropic structure; therefore, we refrain from detailed interpretation in this study.

## 4. Discussion

### 4.1. Segmentation of Deep Crustal Magma Reservoirs Beneath the Cascades Arc

The two LVZs in the mid-lower crust of the region are among our most important findings. The northern branch (LVZ1) is near the previously identified Southern Washington Cascades Conductor (SWCC; Figure 9a) beneath the three volcanoes of Mt. Rainier, MA, and MSH. Multiple magnetotelluric studies interpret a conductivity anomaly here as the signal of a complex of subducted sedimentary rocks associated with Siletzia accretion (Bedrosian et al., 2018; Stanley et al., 1987). Alternatively, Hill et al. (2009) propose that the SWCC may have a magmatic origin. Based on ambient noise adjoint tomography, Flinders and Shen (2017) interpret the SWCC as an extensive region of middle crustal partial melt connecting the three volcanoes (Figure 9a), consistent with the conclusion of Hill et al. (2009). Here, we find a partially overlapping LVZ (LVZ1) that approximately connects MA and Mt. Rainier but becomes subdued between Mt. Rainier and MSH (Figure 9), which is different from Flinders and Shen (2017). A similar LVZ that trends southeast from Mt. Rainier was imaged by P wave tomography at depths of ~14–23 km, below which the earthquake travel time tomography lacked resolution (Moran et al., 1999). The difference in lateral extent of the LVZ1 between the new  $V_s$  model and the  $V_s$  model from Flinders and Shen (2017) coincides with an area of positive anisotropy, which means that this part of the LVZ would be more prominent in purely Rayleigh wave tomography than the isotropic  $V_s$  estimated from Rayleigh and Love waves in this study. We attribute a greater northeastern extent of the LVZ in this study to the larger number of seismographs, with added coverage within and beyond the arc (Figure 1b). Our synthetic tests presented in Figure S7 in Supporting Information S1 show that the anisotropy at mid-lower crust depth can be resolved but the magnitude might be underestimated.

Compared to the northern LVZ, the southern one (LVZ2) extends between Mt. Hood and MSH and is less studied with prior tomography. Its narrower elongated shape may be more difficult to resolve, and this is the first tomography study to integrate the local array surrounding MSH with wider aperture data south of the Columbia River. Interestingly, MSH and Indian Heaven Volcanic Field (marked as a hollow circle in Figures 9a and 9b) are located near the northern periphery of the LVZ2, which shows lower  $V_s$  than the area directly between MSH and MA (Figure 9a). This probably explains why previous 2D models or local scale tomography models observe a subtle mid-lower reservoir directly east of MSH (Figure 10) with absolute  $V_s$  that could be reasonably interpreted as sub-solidus crust if it were not beneath an active volcanic arc (e.g., Crosbie et al., 2019; Kiser et al., 2016, 2018; Ulberg et al., 2020) where heat flow is consistent with deep crustal magma storage (e.g., Blackwell et al., 1990).

Regional examples of mafic and felsic-to-intermediate compositions are used to evaluate the potential properties of the two inferred mid-lower crustal magma reservoirs. We consider the mean  $V_s$  from 15 to 30 km because that is a well-resolved depth range where the anomalies are most clearly observed (Figure 9). The average isotropic  $V_s$  in that depth range is 3.7 km/s in the area shown in Figure 9 and we consider this an estimate of the host rock properties for the sub-arc magmatic system. An average composition of mafic granulite at 950°C (e.g., Rudnick & Fountain, 1995) produces a good fit using the elastic modulus calculator of Abers and Hacker (2016). The relationship between  $V_s$  and melt fraction was estimated following the approach of Chu et al. (2010) with the assumption of effective elastic moduli calculated from a crystalline framework with fluid-saturated pore space, a simplified pressure model and a critical porosity of 30%. Gassmann's (1951) equations and estimated melt properties for basalt and dacite, with variable water contents, illustrate a plausible range of  $V_s$  versus melt fraction relationships. Representative bulk compositions for dacite and basalt were obtained from prior studies at MSH (Wanke et al., 2019). The imaged LVZs with 15–30 km isotropic  $V_s$  of ~3.45–3.55 km/s correspond to melt

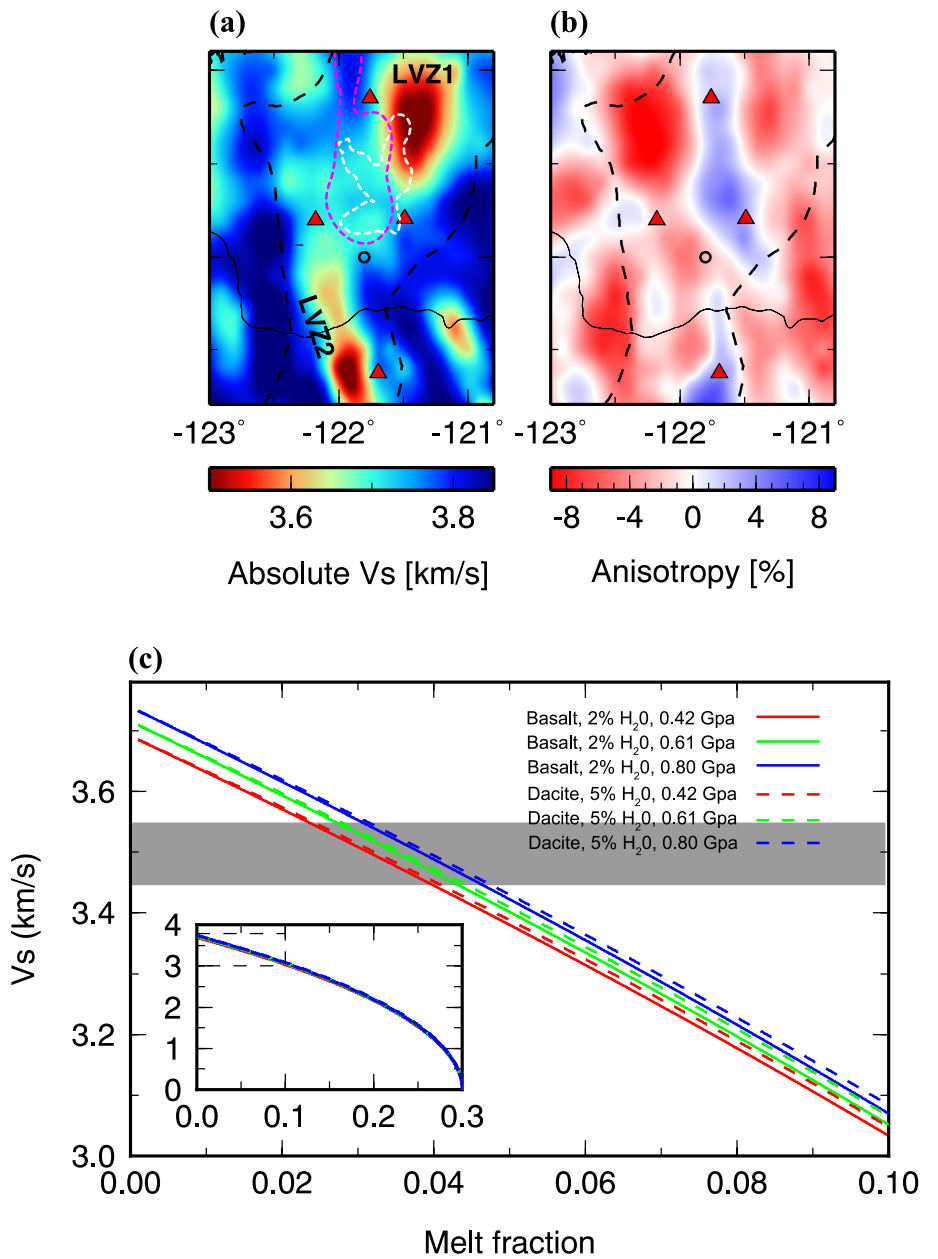


**Figure 9.** Averaged model at 15–30 km depth range for our study region (a) for absolute  $V_s$  and (b) for radial anisotropy. (c) The derived relationships between melt fraction and the absolute  $V_s$ , following the approach of Chu et al. (2010) for basalt and dacite compositions color-coded by the  $\text{H}_2\text{O}$  content and crustal pressure conditions with the assumptions noted in Section 4.1. Black dashed lines in panels (a–b) denote the tectonic boundary of the Cascade Volcanic Arc, the black circles mark the approximate location of the Indian Heaven Volcanic Field (IH) and the red triangles show the four major volcanoes in the region. The two LVZs referred to in Section 4.1 are labeled as LVZ1 and LVZ2, respectively. The white dashed line in panel (a) approximates the 7% velocity reduction contour at a depth of 22 km from Flinders and Shen (2017). The magenta dashed line in panel (a) denotes the location of the Southern Washington Cascades Conductor (Hill et al., 2009). The insert in panel (c) shows the complete range of the relationship with  $V_s$  ranging between 0 and 4 km/s, and the dashed box denotes the zoomed-in portions of the relation shown in the main figure of panel (c). The shaded regions show the major measurements of interest.

fractions of ~2.5%–5% for dacitic or basaltic melt with up to 5 wt% water. If instead of the depth-averaged  $V_s$ , we consider the minimum observed  $V_s$  of ~3.35 km/s at 20 km, then melt fractions up to ~6.5% are predicted. The estimated upper bounds on partial melt in the deep crustal reservoir are lower than the estimates for the upper crustal reservoir at MSH, where controlled source P tomography suggests dacite melt fractions up to ~10%–12%

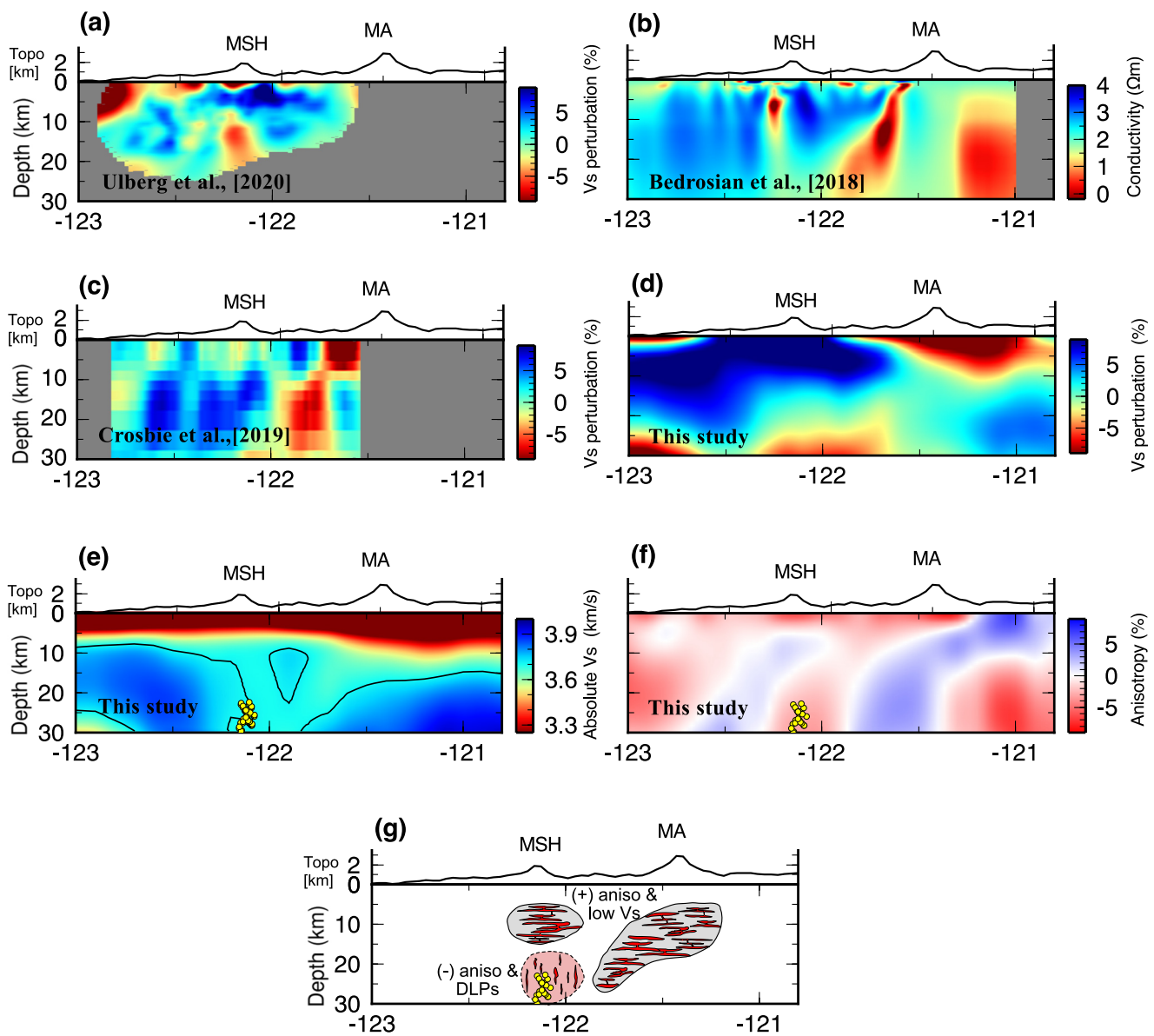


**Figure 10.** Comparison of three existing geophysical models around Mount St. Helens along with our model along the A–A' profile (a–f) and an interpretative cartoon (g). Panel (a) shows the  $V_s$  tomography models from Ulberg et al. (2020); panel (b) shows the Magnetotelluric (MT) result from Bedrosian et al. (2018); panel (c) shows the  $V_s$  tomography models from Crosbie et al. (2019); panels (d)–(f) show our new 3D model with the isotropic component plotted in perturbation (d) and absolute  $V_s$  (e) and the anisotropic component in panel (f), respectively. The yellow filled circles in panels (e–g) denote the deep long-period seismicity (DLPs) from the Pacific Northwest Seismic Network catalog. The gray-shaded regions in panel (g) show positive anisotropy and relatively low  $V_s$ , while the red shaded region shows negative anisotropy with vertically aligned DLPs.

at  $\sim$ 4–6 km depth (Kiser et al., 2018). The melt fraction estimates above consider plausible mean conditions for the deep crust beneath the arc, but actual melt fractions may be more variable on account of heterogeneous composition, temperature, and uncertainties in inferring melt fraction from  $V_s$  imaging.

We note that different models exist for the  $V_s$  versus melt fraction relationship (e.g., Caricchi et al., 2008; Takei, 2002) and that tomography may not accurately recover the full magnitude of the velocity anomaly caused by magma reservoirs (e.g., Maguire, Schmandt, Chen, et al., 2022; Schmandt et al., 2019). One of the most influential parameters for relating seismic velocity to melt fraction is the assumed geometry of melt-filled pore spaces (Takei, 2002). Aspect ratios much less than 0.1, which are associated with disequilibrium systems, could explain the observed  $V_s$  with lower melt fractions (Takei, 2002). In this study, the lowest  $V_s$  volumes do not correspond to the areas of strongest anisotropy suggesting that conditions may be close to textural equilibrium. Still, it is not

possible to know the relevant pore geometry, so the estimates above could be considered upper bounds from the perspective of estimating melt geometry. In contrast, 3D numerical wavefield tests of surface wave tomography methods with synthetic magma reservoir structures indicate that the actual  $V_s$  is likely lower than that recovered by our tomography (Maguire, Schmandt, Chen, et al., 2022). Therefore, there are sources of uncertainty that could bias our estimated melt toward over- or under-estimation, but it is difficult to explain deep crustal  $V_s$  beneath the arc reaching as low as  $\sim 3.35$  km/s without the presence of melt.

The deep crustal LVZs suggest two magmatic segments based on physical properties that control seismic velocities, such as melt fraction, temperature, and bulk composition. Attempts to cluster Cascade arc volcanoes using geochemical data (major and trace elements, isotopic ratios) provide an interesting context for comparison (Mullen et al., 2017; Pitcher & Kent, 2019; Schmidt et al., 2008). For example, a recent geochemical study of Pitcher and Kent (2019) puts MSH, MA, and Mt. Rainier all in the “Washington” cluster but with the Mt. Hood in an ambiguous place. A prior geochemical study placed Mt. Hood, MSH and MA in a common “Columbia” segment and Mt. Rainier in the adjacent “North” segment (Schmidt et al., 2008). In the new seismic tomography results, Mt. Hood and MSH are spatially linked to the southern LVZ, while Mt. Adams and Mt. Rainier are linked to the northern LVZ (Figures 9a and 9b). We suggest that geophysical and geochemical clusters differ because deep crustal reservoirs with modest (up to  $\sim 6\%$ ) melt fractions may not be sufficiently well-mixed to tightly cluster geochemical characteristics. Additionally, common characteristics in deep crustal reservoirs could be obscured by along-strike variations in upper crustal properties that influence the final focusing of magma ascent (e.g., O’Hara et al., 2020).

We propose that the unusual arc-perpendicular positioning of MSH and MA is linked to the segmentation of the deep crustal magma reservoirs, which are sub-parallel but staggered in east-west position, leaving a small gap between them at the latitude of MSH and MA (Figures 9 and 10). However, what controls the shape and location of deep crustal magma reservoirs relative to volcanic vents is another interesting question and multiple hypotheses for the relative importance of shallow and deep structures have been proposed. For example, Bedrosian et al. (2018) argue that the magmatic system, including its deep reservoir and surface expression, might be largely controlled by the inherited crustal structures, a so-called “top-down” mechanism proposed based on a high-resolution resistivity model along the transect connecting MSH and MA. In their model, inherited tectonic boundaries and the extent of deeply buried metasedimentary rocks control the locations of felsic vents with the final ascent influenced by the locations of pre-existing intrusions and crustal faults. In particular, the presence of a resistive pluton in the middle to upper crust may deflect ascending melt west toward Mount St. Helens and east toward MA (Bedrosian et al., 2018). Similarly, the locations of active crustal fault systems, such as the MSH Seismic Zone and West Rainier Seismic Zone, have long been suggested to influence the locations of major vents (Stanley et al., 1996). In contrast, Kiser et al. (2021) proposed a “bottom-up” mechanism that emphasizes the influence of lower crustal structure in modulating the relative buoyancy of melt compared to the surrounding crust, which could focus vents above areas of higher lower crustal velocity and density. Future geodynamic studies of melt migration in actively deforming crust may be able to provide new insights into the relative importance of shallow and deep influences on melt ascent and vent locations.

The organization of sub-arc lower crustal magma reservoirs imaged in this study implies that none of the four stratovolcanoes directly overlie the centroid of their lower crustal magma reservoir. Such lower crustal reservoir offsets are consistent with a recent global compilation indicating that offset reservoir positions become more likely with increasing depth beneath the volcano (Lerner et al., 2020). We note that the scenario of offset lower crustal reservoirs that feed multiple volcanoes poses a challenge for local geophysical imaging studies that intend to image complete subcrustal magmatic systems. Wider aperture imaging studies (e.g., spanning multiple stratovolcanoes) appear valuable for accurately constraining 3D magmatic storage and pathways beneath arc volcanoes.

#### 4.2. Sub-Arc Anisotropy and Implications for Magmatic Pathways

Seismic radial anisotropy represents the dependence of seismic wave speed on the polarization direction of the particle motion and can illuminate structural fabric or layering with fine length scales difficult to resolve in traditional seismic tomography. In the crust, radial anisotropy is often taken as a strong indicator of tectonic deformation as its origin usually involves strain-induced alignments of fractures in the shallow crust and anisotropic crustal minerals and foliations in the mid-lower crust (Almqvist & Mainprice, 2017; Crampin, 1981, 1984; Mainprice & Nicolas, 1989). In volcanic settings, radial anisotropy can provide new insights into potential structural fabrics

related to magma organization such as sill or dike complexes (Chambers et al., 2021; Harmon & Rychert, 2015; Jaxybulatov et al., 2014; Jiang et al., 2018; Lynner et al., 2018; D. Miller et al., 2020).

We image 3%–5% positive anisotropy either directly beneath (i.e., MSH and MA) or slightly shifted to the east (i.e., Mt. Rainier and Mt. Hood) of the volcanic centers at 8–15 km depth range, where shallow magmatic reservoirs are interpreted by higher frequency body wave tomography and magnetotelluric imaging (Figure 10) (Kiser et al., 2018; Ulberg et al., 2020). Positive radial anisotropy is consistent with horizontal layering of heterogeneous seismic velocities (Jaxybulatov et al., 2014), and its appearance within the magmatic reservoirs at shallow depths beneath the four volcanoes probably indicates a crystal-rich magma storage zone organized as a sequence of stacked sills. Similar anisotropic features have been observed in the magmatic reservoirs beneath the Toba, Long Valley, and Yellowstone calderas (Jaxybulatov et al., 2014; Jiang et al., 2018). However, the amplitude of the anisotropy in our study is weaker compared to the large sub-caldera systems (>10%), suggesting smaller reservoirs or less concentrated melt beneath the stratovolcanoes. This is consistent with the ~2.5%–5% melt content inferred from the isotropic  $V_s$ , compared to ~27% melt estimated for Long Valley (Flinders & Shen, 2017) and ~5%–32% for Yellowstone using the same assumptions (Chu et al., 2010; Huang et al., 2015; Maguire, Schmandt, Li, et al., 2022). Given the small width, <10 km, of upper crustal reservoirs indicated by higher frequency body-wave tomography beneath the stratovolcanoes (Kiser et al., 2018; Moran et al., 1999; Ulberg et al., 2020), we expect that the true magnitude of the upper crustal velocity anomalies is not fully recovered by our lower frequency surface wave tomography (e.g., Maguire, Schmandt, Chen, et al., 2022; Paulatto et al., 2022).

Compared to the similar anisotropic features above 20 km depth, different anisotropic signatures are observed deeper beneath the four volcanoes. Mt. Rainier, MA, and Mt. Hood all have positive anisotropy either directly beneath or near the corresponding volcanic centers extending to mid-lower crust depths, likely representing a continuation of the sill complexes. A similar structure of ~6% positive anisotropy is observed beneath the Costa Rica arc at ~15–30 km depth (Harmon & Rychert, 2015). However, the opposite sign of anisotropy, up to –15%, is revealed beneath Colima volcano in Mexico at 15–25 km depth (Spica et al., 2017). Therefore, it remains to be further explored whether the mid-lower crust sill complexes are common features for arc volcanoes or if melt organization is more strongly modulated by other factors such as inherited local crustal structure and active tectonic deformation. We note that the connected anisotropic anomaly between Mt. Rainier and MA is mostly adjacent to the northern LVZ, indicating greater lower crustal magma storage just east of Mt. Rainier and north of MA. The trends of the anisotropy anomalies and the LVZs are almost parallel to the WRSZ and SHZ, suggesting a possible connection between magma migration and the transpressive tectonic strain (Stanley et al., 1996). We suggest that these zones of strain may guide the migration of melt from deep crustal reservoirs into more transient sill complexes beneath specific volcanoes (e.g., Kohlstedt & Holtzman, 2009).

MSH is distinctive because its positive radial anisotropy anomaly dips to the west such that the stratovolcano is underlain by a negative anisotropy at >20 km depth, where it overlaps the southern LVZ. The relatively weak  $V_s$  reductions likely indicate less melt directly beneath the volcano, making the relatively weak anisotropy even more challenging to resolve. This region of lower-crust negative anisotropy is coincident with frequent deep long-period events (Figures 10e and 10f), whose occurrence is interpreted to reflect the vertical transport of fluids and/or magma (Kiser et al., 2016; Nichols et al., 2011). The negative anisotropy beneath MSH terminates before reaching Mount Hood in the south. Negative radial anisotropy has also been previously detected in several other volcanic systems, including Piton de la Fournaise, Colima, and Okmok, and is interpreted to represent concentrations of dikes responsible for rapid magma transport (D. Miller et al., 2020; Mordret et al., 2015; Spica et al., 2017). A similar structure here could suggest a more prevalent magma transport through dikes beneath MSH (Figure 10g) compared to the other three volcanoes of Mt. Rainier, Mt. Adam, and Mt. Hood.

## 5. Conclusions

Ambient seismic noise data from 234 temporary and permanent seismographs in the central to the northern Cascades arc were used to image the deep crustal magmatic system. Combined Rayleigh and Love tomography constrain isotropic  $V_s$  and identify radially anisotropic structures. New isotropic  $V_s$  images revealed two sub-parallel mid-lower crust magma reservoir segments that span multiple stratovolcanoes. One approximately spans from Mt. Rainier to MA and the other from MSH to Mt. Hood. Based on our  $V_s$  results, some strict assumptions about magma geometry and basement composition, and previously erupted compositions, ~2.5%–6% melt was estimated for the mid-lower crust reservoirs assuming near equilibrium melt geometry. Mid-lower

crustal radial anisotropy is important for fitting Rayleigh and Love wave dispersion and estimating isotropic  $V_s$  beneath the Cascades arc. Positive radial anisotropy volumes underlie all four volcanoes at 10–20 km depths and are adjacent to the mid-lower crust isotropic LVZs, possibly reflecting the lateral movement of magma from the larger mid-lower crust reservoirs into mostly crystallized sill complexes beneath specific volcanoes. Positive anisotropy extends to the lower crust beneath Mt. Rainier, MA, and Mt. Hood. Beneath MSH, the positive anisotropy volume dips to the west such that the volcano is underlain by negative anisotropy in the mid-lower crust, suggesting a transition to more dike structures.

The presence of two sub-parallel mid-lower crustal magma reservoirs of  $V_s \sim 3.4\text{--}3.55$  km/s that are staggered in their east-west positions may help explain why two stratovolcanoes, MSH and MA, are present at the same position along strike. MSH lies at the northern end of the southern deep crustal magma reservoir segment, while MA lies at the southern end of the northern magma reservoir segment. Thus, our results suggest that deep crustal magma reservoirs or hot zones influence the positions of major arc volcanoes, but a given reservoir may fuel multiple stratovolcanoes with horizontal positions that are offset from the centroid of the reservoir.

## Data Availability Statement

The raw seismic data used in this study are downloaded from IRIS DMC (<https://ds.iris.edu/ds/nodes/dmc>), including following seismic networks: (a) the XD (Creager, 2014); (b) the XU (Malone et al., 2006); (c) the YW (Brudzinski & Allen, 2007); (d) the XC (James & Fouch, 2006); (e) the XQ (Levander, 2007); (f) the TA (IRIS Transportable Array, 2003); (g) the US (Albuquerque Seismological Laboratory (ASL)/USGS, 1990); (h) the UW (University of Washington, 1963); and (i) the ZG (Humphreys, 2006). Figures were produced using the Generic Mapping Tools (Wessel et al., 2013). The NoisePy used in this study for data download and cross-correlation calculation is available on GitHub (<https://zenodo.org/badge/latestdoi/276578127>). The FTAN package used to measure the dispersion information can be found at <http://ciei.colorado.edu/Products/>. The PV-based surface wave inversion code used in this study is available on GitHub (<https://zenodo.org/badge/latestdoi/248079180>).

## Acknowledgments

The authors thank the editor Dr. Marie Edmonds and the two anonymous reviewers for their comments that helped improve the manuscript. The IRIS Data Management Center was used to access seismic data. A complete list of the seismic networks and their full citations are provided in the Data Availability Statement. The IRIS DMC was supported by the National Science Foundation under the Cooperative Support Agreement EAR-1851048. This research was supported by the NSF EAR-1554908 and EAR-1950328, as well as the Australian Research Council through the Discovery Grant Program (DP150102887). Chengxin Jiang acknowledges the financial support from the Discovery Early Career Research Award from the Australian Research Council (DE220100907).

## References

- Abers, G. A., & Hacker, B. R. (2016). A MATLAB toolbox and Excel workbook for calculating the densities, seismic wave speeds, and major element composition of minerals and rocks at pressure and temperature. *Geochemistry, Geophysics, Geosystems*, 17(2), 616–624. <https://doi.org/10.1002/2015gc006171>
- Albuquerque Seismological Laboratory (ASL)/USGS. (1990). United States National Seismic Network [Dataset]. International Federation of Digital Seismograph Networks. <https://doi.org/10.7914/SN/US>
- Almqvist, B. S., & Mainprice, D. (2017). Seismic properties and anisotropy of the continental crust: Predictions based on mineral texture and rock microstructure. *Reviews of Geophysics*, 55(2), 367–433. <https://doi.org/10.1002/2016rg000552>
- Bedrosian, P. A., Peacock, J. R., Bowles-Martinez, E., Schultz, A., & Hill, G. J. (2018). Crustal inheritance and a top-down control on arc magmatism at Mount St Helens. *Nature Geoscience*, 11(11), 865–870. <https://doi.org/10.1038/s41561-018-0217-2>
- Bensen, G. D., Ritzwoller, M. H., Barmin, M. P., Levshin, A. L., Lin, F., Moschetti, M. P., et al. (2007). Processing seismic ambient noise data to obtain reliable broad-band surface wave dispersion measurements. *Geophysical Journal International*, 169(3), 1239–1260. <https://doi.org/10.1111/j.1365-246x.2007.03374.x>
- Blackwell, D. D., Steele, J. L., Kelley, S., & Korosec, M. A. (1990). Heat flow in the state of Washington and thermal conditions in the Cascade Range. *Journal of Geophysical Research*, 95(B12), 19495–19516. <https://doi.org/10.1029/jb095ib12p19495>
- Bostock, M. G. (2013). The Moho in subduction zones. *Tectonophysics*, 609, 547–557. <https://doi.org/10.1016/j.tecto.2012.07.007>
- Brocher, T. M. (2005). Empirical relations between elastic wavespeeds and density in the Earth's crust. *Bulletin of the Seismological Society of America*, 95(6), 2081–2092. <https://doi.org/10.1785/0120050077>
- Brocher, T. M., Parsons, T., Tréhu, A. M., Snell, C. M., & Fisher, M. A. (2003). Seismic evidence for widespread serpentinized forearc upper mantle along the Cascadia margin. *Geology*, 31(3), 267–270. [https://doi.org/10.1130/0091-7613\(2003\)031<0267:sefs>2.0.co;2](https://doi.org/10.1130/0091-7613(2003)031<0267:sefs>2.0.co;2)
- Brudzinski, M., & Allen, R. (2007). Resolving structural control of episodic tremor and slip along the length of Cascadia [Dataset]. International Federation of Digital Seismograph Networks. [https://doi.org/10.7914/SN/YW\\_2007](https://doi.org/10.7914/SN/YW_2007)
- Calvert, A. J., Bostock, M. G., Savard, G., & Unsworth, M. J. (2020). Cascadia low frequency earthquakes at the base of an overpressured subduction shear zone. *Nature Communications*, 11(1), 1–10. <https://doi.org/10.1038/s41467-020-17609-3>
- Caricchi, L., Burlini, L., & Ulmer, P. (2008). Propagation of P and S-waves in magmas with different crystal contents: Insights into the crystallinity of magmatic reservoirs. *Journal of Volcanology and Geothermal Research*, 178(4), 740–750. <https://doi.org/10.1016/j.jvolgeores.2008.09.006>
- Cashman, K. V., Sparks, R. S. J., & Blundy, J. D. (2017). Vertically extensive and unstable magmatic systems: A unified view of igneous processes. *Science*, 355(6331), eaag3055. <https://doi.org/10.1126/science.aag3055>
- Chambers, E. L., Harmon, N., Rychert, C. A., & Keir, D. (2021). Variations in melt emplacement beneath the northern East African Rift from radial anisotropy. *Earth and Planetary Science Letters*, 573, 117150. <https://doi.org/10.1016/j.epsl.2021.117150>
- Chu, R., Helmberger, D. V., Sun, D., Jackson, J. M., & Zhu, L. (2010). Musky magma beneath Yellowstone. *Geophysical Research Letters*, 37(1), L01306. <https://doi.org/10.1029/2009gl041656>
- Crampin, S. (1981). A review of wave motion in anisotropic and cracked elastic-media. *Wave Motion*, 3(4), 343–391. [https://doi.org/10.1016/0165-2125\(81\)90026-3](https://doi.org/10.1016/0165-2125(81)90026-3)
- Crampin, S. (1984). Effective anisotropic elastic constants for wave propagation through cracked solids. *Geophysical Journal International*, 76(1), 135–145. <https://doi.org/10.1111/j.1365-246x.1984.tb05029.x>

- Creager, K. (2014). Collaborative Research: Illuminating the architecture of the greater Mount St. Helens magmatic systems from slab to surface [Dataset]. International Federation of Digital Seismograph Networks. [https://doi.org/10.7914/SN/XD\\_2014](https://doi.org/10.7914/SN/XD_2014)
- Crosbie, K. J., Abers, G. A., Mann, M. E., Janiszewski, H. A., Creager, K. C., Ulberg, C. W., & Moran, S. C. (2019). Shear velocity structure from ambient noise and teleseismic surface wave tomography in the cascades around Mount St. Helens. *Journal of Geophysical Research: Solid Earth*, 124(8), 8358–8375. <https://doi.org/10.1029/2019jb017836>
- Delph, J. R., Levander, A., & Niu, F. (2018). Fluid controls on the heterogeneous seismic characteristics of the Cascadia margin. *Geophysical Research Letters*, 45(20), 11–021. <https://doi.org/10.1029/2018gl079518>
- Eakin, C. M., Wirth, E. A., Wallace, A., Ulberg, C. W., Creager, K. C., & Abers, G. A. (2019). SKS splitting beneath Mount St. Helens: Constraints on subslab mantle entrainment. *Geochemistry, Geophysics, Geosystems*, 20(8), 4202–4217. <https://doi.org/10.1029/2019gc008433>
- Ekström, G. (2011). A global model of Love and Rayleigh surface wave dispersion and anisotropy, 25–250 s. *Geophysical Journal International*, 187(3), 1668–1686. <https://doi.org/10.1111/j.1365-246x.2011.05225.x>
- Fang, H., Van Der Hilst, R. D., de Hoop, M. V., Kothari, K., Gupta, S., & Dokmanić, I. (2020). Parsimonious seismic tomography with Poisson Voronoi projections: Methodology and validation. *Seismological Research Letters*, 91(1), 343–355. <https://doi.org/10.1785/0220190141>
- Flinders, A. F., & Shen, Y. (2017). Seismic evidence for a possible deep crustal hot zone beneath Southwest Washington. *Scientific Reports*, 7(1), 1–10. <https://doi.org/10.1038/s41598-017-07123-w>
- Gassmann, F. (1951). Elastic waves through a packing of spheres. *Geophysics*, 16(4), 673–685. <https://doi.org/10.1190/1.1437718>
- Harmon, N., & Rychert, C. A. (2015). Seismic imaging of deep crustal melt sills beneath Costa Rica suggests a method for the formation of the Archean continental crust. *Earth and Planetary Science Letters*, 430, 140–148. <https://doi.org/10.1016/j.epsl.2015.07.062>
- Hayes, G. P., Moore, G. L., Portner, D. E., Hearne, M., Flamme, H., Furtney, M., & Smoczyk, G. M. (2018). Slab2, a comprehensive subduction zone geometry model. *Science*, 362(6410), 58–61. <https://doi.org/10.1126/science.aat4723>
- Herrmann, R. B. (2013). Computer programs in seismology: An evolving tool for instruction and research. *Seismological Research Letters*, 84(6), 1081–1088. <https://doi.org/10.1785/0220110096>
- Hildreth, W. (2007). *Quaternary magmatism in the Cascades: Geologic perspectives*. US Geological Survey.
- Hill, G. J., Caldwell, T. G., Heise, W., Chertkoff, D. G., Bibby, H. M., Burgess, M. K., et al. (2009). Distribution of melt beneath Mount St. Helens and Mount Adams inferred from magnetotelluric data. *Nature Geoscience*, 2(11), 785–789. <https://doi.org/10.1038/geo661>
- Huang, H. H., Lin, F. C., Schmandt, B., Farrell, J., Smith, R. B., & Tsai, V. C. (2015). The Yellowstone magmatic system from the mantle plume to the upper crust. *Science*, 348(6236), 773–776. <https://doi.org/10.1126/science.aaa5648>
- Humphreys, G. (2006). Origin of the Columbia River Basalts and Uplift of the Wallowa Mountains [Dataset]. International Federation of Digital Seismograph Networks. [https://doi.org/10.7914/SN/ZG\\_2006](https://doi.org/10.7914/SN/ZG_2006)
- IRIS Transportable Array. (2003). USAArray transportable array [Dataset]. International Federation of Digital Seismograph Networks. <https://doi.org/10.7914/SN/TA>
- James, D., & Fouch, M. (2006). Collaborative research: Understanding the causes of continental intraplate tectonomagmatism: A case study in the Pacific Northwest [Dataset]. International Federation of Digital Seismograph Networks. [https://doi.org/10.7914/SN/XC\\_2006](https://doi.org/10.7914/SN/XC_2006)
- Jaxybulatov, K., Shapiro, N. M., Koulakov, I., Mordret, A., Landès, M., & Sens-Schönfelder, C. (2014). A large magmatic sill complex beneath the Toba caldera. *Science*, 346(6209), 617–619. <https://doi.org/10.1126/science.1258582>
- Jiang, C., & Denolle, M. A. (2020). NoisePy: A new high-performance python tool for ambient-noise seismology. *Seismological Research Letters*, 91(3), 1853–1866. <https://doi.org/10.1785/0220190364>
- Jiang, C., Schmandt, B., Farrell, J., Lin, F. C., & Ward, K. M. (2018). Seismically anisotropic magma reservoirs underlying silicic calderas. *Geology*, 46(8), 727–730. <https://doi.org/10.1130/g45104.1>
- Kanamori, H., & Anderson, D. L. (1977). Importance of physical dispersion in surface wave and free oscillation problems. *Reviews of Geophysics*, 15(1), 105–112. <https://doi.org/10.1029/rg015i001p00105>
- Kiser, E., Levander, A., Schmandt, B., & Hansen, S. (2021). Seismic evidence of bottom-up crustal control on volcanism and magma storage near Mount St. Helens. *Geophysical Research Letters*, 48(5), e2020GL090612. <https://doi.org/10.1029/2020GL090612>
- Kiser, E., Levander, A., Zelt, C., Schmandt, B., & Hansen, S. (2018). Focusing of melt near the top of the Mount St. Helens (USA) magma reservoir and its relationship to major volcanic eruptions. *Geology*, 46(9), 775–778. <https://doi.org/10.1130/g45140.1>
- Kiser, E., Palomeras, I., Levander, A., Zelt, C., Harder, S., Schmandt, B., et al. (2016). Magma reservoirs from the upper crust to the Moho inferred from high-resolution Vp and Vs models beneath Mount St. Helens, Washington State, USA. *Geology*, 44(6), 411–414. <https://doi.org/10.1130/g37591.1>
- Kohlstedt, D. L., & Holtzman, B. K. (2009). Shearing melt out of the Earth: An experimentalist's perspective on the influence of deformation on melt extraction. *Annual Review of Earth and Planetary Sciences*, 37(1), 561–593. <https://doi.org/10.1146/annurev.earth.031208.100104>
- Lee, C., & Wada, I. (2017). Clustering of arc volcanoes caused by temperature perturbations in the back-arc mantle. *Nature Communications*, 8(1), 1–9. <https://doi.org/10.1038/ncomms15753>
- Lerner, A. H., O'Hara, D., Karlstrom, L., Ebmeier, S. K., Anderson, K. R., & Hurwitz, S. (2020). The prevalence and significance of offset magma reservoirs at arc volcanoes. *Geophysical Research Letters*, 47(14), e2020GL087856. <https://doi.org/10.1029/2020gl087856>
- Levander, A. (2007). Seismic and geodetic investigations of Mendocino Triple junction dynamics [Dataset]. International Federation of Digital Seismograph Networks. [https://doi.org/10.7914/SN/XQ\\_2007](https://doi.org/10.7914/SN/XQ_2007)
- Levshin, A. L., & Ritzwoller, M. H. (2001). Automated detection, extraction, and measurement of regional surface waves. In *Monitoring the comprehensive nuclear-test-ban treaty: Surface waves* (pp. 1531–1545). Birkhäuser.
- Lin, F. C., Moschetti, M. P., & Ritzwoller, M. H. (2008). Surface wave tomography of the western United States from ambient seismic noise: Rayleigh and Love wave phase velocity maps. *Geophysical Journal International*, 173(1), 281–298. <https://doi.org/10.1111/j.1365-246x.2008.03720.x>
- Luo, Y., Yang, Y., Xu, Y., Xu, H., Zhao, K., & Wang, K. (2015). On the limitations of interstation distances in ambient noise tomography. *Geophysical Journal International*, 201(2), 652–661. <https://doi.org/10.1093/gji/ggv043>
- Lynner, C., Beck, S. L., Zandt, G., Porritt, R. W., Lin, F. C., & Eilon, Z. C. (2018). Midcrustal deformation in the Central Andes constrained by radial anisotropy. *Journal of Geophysical Research: Solid Earth*, 123(6), 4798–4813. <https://doi.org/10.1029/2017jb014936>
- Maguire, R., Schmandt, B., Chen, M., Jiang, C., Li, J., & Wilgus, J. (2022). Resolving continental magma reservoirs with 3D surface wave tomography. *Geochemistry, Geophysics, Geosystems*, 23(8), e2022GC010446. <https://doi.org/10.1029/2022gc010446>
- Maguire, R., Schmandt, B., Li, J., Jiang, C., Li, G., Wilgus, J., & Chen, M. (2022). Magma accumulation at depths of prior rhyolite storage beneath Yellowstone Caldera. *Science*, 378(6623), 1001–1004. <https://doi.org/10.1126/science.adc0347>
- Mainprice, D., & Nicolas, A. (1989). Development of shape and lattice preferred orientations: Application to the seismic anisotropy of the lower crust. *Journal of Structural Geology*, 11(1–2), 175–189. [https://doi.org/10.1016/0191-8141\(89\)90042-4](https://doi.org/10.1016/0191-8141(89)90042-4)

- Malone, S., Creager, K., Rondenay, S., Melbourne, T., & Abers, G. (2006). Collaborative Research: Earthscope integrated investigations of Cascadia subduction zone tremor, structure and process [Dataset]. International Federation of Digital Seismograph Networks. [https://doi.org/10.7914/SN/XU\\_2006](https://doi.org/10.7914/SN/XU_2006)
- McGary, R. S., Evans, R. L., Wannamaker, P. E., Elsenbeck, J., & Rondenay, S. (2014). Pathway from subducting slab to surface for melt and fluids beneath Mount Rainier. *Nature*, 511(7509), 338–340. <https://doi.org/10.1038/nature13493>
- Miller, D., Bennington, N., Haney, M., Bedrosian, P., Key, K., Thurber, C., et al. (2020). Linking magma storage and ascent to eruption volume and composition at an arc caldera. *Geophysical Research Letters*, 47(14), e2020GL088122. <https://doi.org/10.1029/2020gl088122>
- Miller, K. C., Keller, G. R., Gridley, J. M., Luetgert, J. H., Mooney, W. D., & Thybo, H. (1997). Crustal structure along the west flank of the Cascades, western Washington. *Journal of Geophysical Research*, 102(B8), 17857–17873. <https://doi.org/10.1029/97jb00882>
- Moran, S. C., Lees, J. M., & Malone, S. D. (1999). P wave crustal velocity structure in the greater Mount Rainier area from local earthquake tomography. *Journal of Geophysical Research*, 104(B5), 10775–10786. <https://doi.org/10.1029/1999jb900036>
- Mordret, A., Rivet, D., Landès, M., & Shapiro, N. M. (2015). Three-dimensional shear velocity anisotropic model of Piton de la Fournaise Volcano (La Réunion Island) from ambient seismic noise. *Journal of Geophysical Research: Solid Earth*, 120(1), 406–427. <https://doi.org/10.1002/2014jb011654>
- Moschetti, M. P., Ritzwoller, M. H., Lin, F., & Yang, Y. (2010). Seismic evidence for widespread western-US deep-crustal deformation caused by extension. *Nature*, 464(7290), 885–889. <https://doi.org/10.1038/nature08951>
- Mosegaard, K., & Tarantola, A. (1995). Monte Carlo sampling of solutions to inverse problems. *Journal of Geophysical Research*, 100(B7), 12431–12447. <https://doi.org/10.1029/94jb03097>
- Mullen, E. K., Weis, D., Marsh, N. B., & Martindale, M. (2017). Primitive arc magma diversity: New geochemical insights in the Cascade Arc. *Chemical Geology*, 448, 43–70. <https://doi.org/10.1016/j.chemgeo.2016.11.006>
- Nichols, M. L., Malone, S. D., Moran, S. C., Thelen, W. A., & Vidale, J. E. (2011). Deep long-period earthquakes beneath Washington and Oregon volcanoes. *Journal of Volcanology and Geothermal Research*, 200(3–4), 116–128. <https://doi.org/10.1016/j.jvolgeores.2010.12.005>
- O'Hara, D., Karlstrom, L., & Ramsey, D. W. (2020). Time-evolving surface and subsurface signatures of Quaternary volcanism in the Cascades arc. *Geology*, 48(11), 1088–1093. <https://doi.org/10.1130/g47706.1>
- Parsons, T., Trehu, A. M., Luetgert, J. H., Miller, K., Kilbride, F., Wells, R. E., et al. (1998). A new view into the Cascadia subduction zone and volcanic arc: Implications for earthquake hazards along the Washington margin. *Geology*, 26(3), 199–202. [https://doi.org/10.1130/0091-7613\(1998\)026<0199:avanc>2.3.co;2](https://doi.org/10.1130/0091-7613(1998)026<0199:avanc>2.3.co;2)
- Paulatto, M., Hoot, E., Chrapkiewicz, K., Heath, B., Toomey, D., & Morgan, J. (2022). Advances in seismic imaging of magma and crystal mush. *Frontiers of Earth Science*, 10, 1–31. <https://doi.org/10.3389/feart.2022.970131>
- Pitcher, B. W., & Kent, A. J. (2019). Statistics and segmentation: Using big data to assess cascades arc compositional variability. *Geochimica et Cosmochimica Acta*, 265, 443–467. <https://doi.org/10.1016/j.gca.2019.08.035>
- Rawlinson, N., & Spakman, W. (2016). On the use of sensitivity tests in seismic tomography. *Geophysical Journal International*, 205(2), 1221–1243. <https://doi.org/10.1093/gji/ggw084>
- Rudnick, R. L., & Fountain, D. M. (1995). Nature and composition of the continental crust: A lower crustal perspective. *Reviews of Geophysics*, 33(3), 267–309. <https://doi.org/10.1029/95rg01302>
- Schmandt, B., Jiang, C., & Farrell, J. (2019). Seismic perspectives from the western US on magma reservoirs underlying large silicic calderas. *Journal of Volcanology and Geothermal Research*, 384, 158–178. <https://doi.org/10.1016/j.jvolgeores.2019.07.015>
- Schmandt, B., Lin, F. C., & Karlstrom, K. E. (2015). Distinct crustal isostasy trends east and west of the Rocky Mountain Front. *Geophysical Research Letters*, 42(23), 10–290. <https://doi.org/10.1002/2015gl066593>
- Schmidt, M. E., Gruner, A. L., & Rowe, M. C. (2008). Segmentation of the Cascade Arc as indicated by Sr and Nd isotopic variation among diverse primitive basalts. *Earth and Planetary Science Letters*, 266(1–2), 166–181. <https://doi.org/10.1016/j.epsl.2007.11.013>
- Seats, K. J., Lawrence, J. F., & Prieto, G. A. (2012). Improved ambient noise correlation functions using Welch's method. *Geophysical Journal International*, 188(2), 513–523. <https://doi.org/10.1111/j.1365-246x.2011.05263.x>
- Shen, W., Ritzwoller, M. H., Schulte-Pelkum, V., & Lin, F. C. (2013). Joint inversion of surface wave dispersion and receiver functions: A Bayesian Monte-Carlo approach. *Geophysical Journal International*, 192(2), 807–836. <https://doi.org/10.1093/gji/ggs050>
- Spica, Z., Perton, M., & Legrand, D. (2017). Anatomy of the Colima volcano magmatic system, Mexico. *Earth and Planetary Science Letters*, 459, 1–13. <https://doi.org/10.1016/j.epsl.2016.11.010>
- Stanley, W. D., Finn, C., & Plesha, J. L. (1987). Tectonics and conductivity structures in the southern Washington Cascades. *Journal of Geophysical Research*, 92(B10), 10179–10193. <https://doi.org/10.1029/JB092iB10p10179>
- Stanley, W. D., Johnson, S. Y., Qamar, A. I., Weaver, C. S., & Williams, J. M. (1996). Tectonics and seismicity of the southern Washington Cascade Range. *Bulletin of the Seismological Society of America*, 86(1A), 1–18. <https://doi.org/10.1785/BSSA08601A0001>
- Takei, Y. (2002). Effect of pore geometry on  $V_p/V_s$ : From equilibrium geometry to crack. *Journal of Geophysical Research*, 107(B2), ECV-6.
- Till, C. B., Kent, A. J. R., Abers, G. A., Janiszewski, H. A., Gaherty, J. B., & Pitcher, B. W. (2019). The causes of spatiotemporal variations in erupted fluxes and compositions along a volcanic arc. *Nature Communications*, 10(1), 1–12. <https://doi.org/10.1038/s41467-019-10113-0>
- Ulberg, C. W., Creager, K. C., Moran, S. C., Abers, G. A., Thelen, W. A., Levander, A., et al. (2020). Local source  $V_p$  and  $V_s$  tomography in the Mount St. Helens region with the iMUSH broadband array. *Geochemistry, Geophysics, Geosystems*, 21(3), e2019GC008888. <https://doi.org/10.1029/2019gc008888>
- University of Washington. (1963). Pacific Northwest Seismic Network – University of Washington [Dataset]. International Federation of Digital Seismograph Networks. <https://doi.org/10.7914/SN/UW>
- Wanke, M., Clyne, M. A., von Quadrt, A., Vennemann, T. W., & Bachmann, O. (2019). Geochemical and petrological diversity of mafic magmas from Mount St. Helens. *Contributions to Mineralogy and Petrology*, 174(1), 10. <https://doi.org/10.1007/s00410-018-1544-4>
- Wells, R., Bukry, D., Friedman, R., Pyle, D., Duncan, R., Haeussler, P., & Wooden, J. (2014). Geologic history of Siletzia, a large igneous province in the Oregon and Washington Coast Range: Correlation to the geomagnetic polarity time scale and implications for a long-lived Yellowstone hotspot. *Geosphere*, 10(4), 692–719. <https://doi.org/10.1130/ges01018.1>
- Wells, R. E., Blakely, R. J., Wech, A. G., McCrary, P. A., & Michael, A. (2017). Cascadia subduction tremor muted by crustal faults. *Geology*, 45(6), 515–518. <https://doi.org/10.1130/g38835.1>
- Wells, R. E., & McCaffrey, R. (2013). Steady rotation of the Cascade arc. *Geology*, 41(9), 1027–1030. <https://doi.org/10.1130/g34514.1>
- Wessel, P., Smith, W. H., Scharrroo, R., Luis, J., & Wobbe, F. (2013). Generic mapping tools: Improved version released. *Eos, Transactions American Geophysical Union*, 94(45), 409–410. <https://doi.org/10.1029/2013eo450001>
- White, M. C., Fang, H., Nakata, N., & Ben-Zion, Y. (2020). PyKonal: A Python package for solving the eikonal equation in spherical and Cartesian coordinates using the fast marching method. *Seismological Research Letters*, 91(4), 2378–2389. <https://doi.org/10.1785/0220190318>

- Wilgus, J., Jiang, C., & Schmandt, B. (2020). A middle crustal channel of radial anisotropy beneath the northeastern Basin and range. *Tectonics*, 39(7), e2020TC006140. <https://doi.org/10.1029/2020tc006140>
- Williams, D. L., & Finn, C. (1987). Evidence for a shallow pluton beneath the Goat Rocks Wilderness, Washington, from gravity and magnetic data. *Journal of Geophysical Research*, 92(B6), 4867–4880. <https://doi.org/10.1029/jb092ib06p04867>
- Xie, J., Ritzwoller, M. H., Brownlee, S. J., & Hacker, B. R. (2015). Inferring the oriented elastic tensor from surface wave observations: Preliminary application across the western United States. *Geophysical Journal International*, 201(2), 996–1021. <https://doi.org/10.1093/gji/ggv054>

## References From the Supporting Information

- Buehler, J. S., & Shearer, P. M. (2017). Uppermost mantle seismic velocity structure beneath USArray. *Journal of Geophysical Research: Solid Earth*, 122(1), 436–448. <https://doi.org/10.1002/2016jb013265>
- Hacker, B. R., Kelemen, P. B., & Behn, M. D. (2015). Continental lower crust. *Annual Review of Earth and Planetary Sciences*, 43(1), 167–205. <https://doi.org/10.1146/annurev-earth-050212-124117>
- Julia, J., Ammon, C. J., Herrmann, R. B., & Correig, A. M. (2000). Joint inversion of receiver function and surface wave dispersion observations. *Geophysical Journal International*, 143(1), 99–112. <https://doi.org/10.1046/j.1365-246x.2000.00217.x>
- Ma, X., & Lowry, A. R. (2017). USArray imaging of continental crust in the conterminous United States. *Tectonics*, 36(12), 2882–2902. <https://doi.org/10.1002/2017tc004540>
- Mann, M. E., Abers, G. A., Crosbie, K., Creager, K., Ulberg, C., Moran, S., & Rondenay, S. (2019). Imaging subduction beneath Mount St. Helens: Implications for slab dehydration and magma transport. *Geophysical Research Letters*, 46(6), 3163–3171. <https://doi.org/10.1029/2018gl081471>
- Shen, W., & Ritzwoller, M. H. (2016). Crustal and uppermost mantle structure beneath the United States. *Journal of Geophysical Research: Solid Earth*, 121(6), 4306–4342. <https://doi.org/10.1002/2016jb012887>
- Tréhu, A. M., Asudeh, I., Brocher, T. M., Luetgert, J. H., Mooney, W. D., Nabelek, J. L., & Nakamura, Y. (1994). Crustal architecture of the Cascadia forearc. *Science*, 266(5183), 237–243. <https://doi.org/10.1126/science.266.5183.237>